MASTER THESIS

Investigation of heavy-flavor jet structures with the ALICE experiment

László Gyulai

Supervisor: **Dr. Róbert Vértesi**

Senior research fellow

Department of High Energy Physics

Wigner Research Centre for Physics

Consultant: **Dr. Dániel Péter Kis**

Associate Professor

Institute of Nuclear Techniques

Budapest University of Technology and Economics

BME

2020

Témakiírás

A CERN nemzetközi kutatóközpont LHC gyorsítója az erős kölcsönhatás alapvető természetét vizsgálja nagy sebességre felgyorsított protonok illetve nehézionok ütköztetése segítségével. Ezekben a nagyenergiás ütközésekben a nehéz (charm és beauty) kvarkok a reakció korai fázisában, ún. kemény folyamatokban keletkeznek, és a folyamat későbbi állapotaiban is megmaradnak, így a segítségükkel a kvantumszíndinamikai elméletek érvényessége, valamint a nehézion-ütközésben létrejövő erősen kölcsönható forró közeg tulajdonságai is vizsgálhatóak. Az LHC 2015-ben indult Run-II adatgyűjtési periódusában a továbbfejlesztett ALICE detektorrendszer segítségével a nehéz kvarkok minden korábbinál pontosabb mérése vált lehetővé. A jelentkező feladata, hogy az LHC Run-II fázisából származó ALICE proton-proton és proton-ólom ütközések kiértékelése, elsősorban a maganyagnak a nehéz kvarkokból keletkező kollimált részecskezáporok (az úgynevezett jetek) szerkezetére gyakorolt hatásának megismerése korrelációs és jetrekonstrukciós mérési módszerekkel. A jelentkező ezáltal a világ egyik vezető nagykísérletének működéséhez és eredményességéhez járul hozzá.

Research topic

The Large Hadron Collider, located in the CERN international research centre, investigates the fundamental nature of strong interaction using protons and heavy-ions accelerated to ultrarelativistic velocities. Heavy flavor (charm and beauty) quarks are produced early in the reaction, and they survive throughout the later stages. Thus, heavy flavor is a perfect tool to test the validity of Quantum Chromodynamics calculations, as well as to research the properties of the hot, strongly interacting medium that is created in heavy-ion collisions. The Run-II data taking period at the LHC brought increased luminosity and an upgraded ALICE detector system. It allows for an unprecedented precision in the measurement of heavy quarks. The task of the applicant is to evaluate proton-proton and proton-lead collisions collected by the ALICE experiment during the LHC Run-II period, focusing on the influence of the nuclear matter on the structure of particle jets originating from the heavy quarks, using correlation and jet reconstruction methods. This way the applicant will participate in one of the world's leading experiments, and contributes to the success of its research program.

Önállósági nyilatkozat

Alulírott Gyulai László a Budapesti Műszaki és Gazdaságtudományi Egyetem fizikus MSc szakos hallgatója kijelentem, hogy ezt a diplomamunkát meg nem engedett segédeszközök nélkül, önállóan, a témavezető irányításával készítettem, és csak a megadott forrásokat használtam fel. Minden olyan részt, melyet szó szerint, vagy azonos értelemben, de átfogalmazva más forrásból vettem, a forrás megadásával jelöltem.

Budapest, 2020.05.28

Contents

1 Introduction

1.1 Standard Model

The second half of the 20th century is known for its breakthroughs in the field of elementary particle physics. To unify all the discoveries into one theory a Standard Model (SM) of particle physics was developed. It describes three out of four known interactions between particles: weak, strong and electromagnetic, while gravity is not a part of the SM. The SM is a gauge theory based on local symmetries of the Lagrangian. Many of the particles that were unknown at the time of the development of the SM were predicted based on these symmetries. All the missing particles were discovered in span of the next decades.
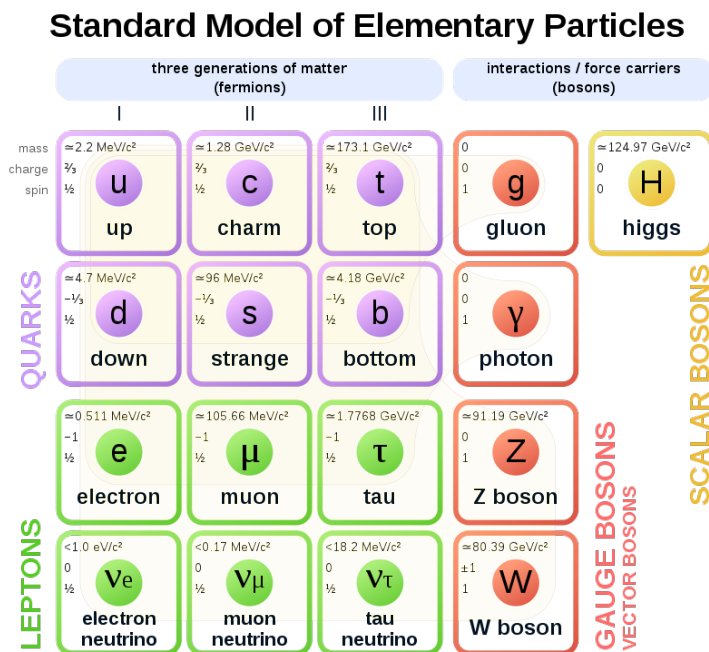
Figure 1: Standard Model of particle physics with three generations of elementary quarks and leptons, as well as bosons [1].

There are a total of 17 particles described by the SM: 6 leptons, 6 quarks, 4 vector bosons and 1 scalar boson (Fig. 1). Leptons and quarks are split into three groups, called generations, which differ only in the particle masses and quantum numbers, called flavors. All leptons and quarks have corresponding anti-particles with the same physical properties, except the charge, which has an opposite value.

Leptons are spin-$\frac{1}{2}$ particles, known as fermions. Each generation of leptons consists of

a heavier particle with charge -1 and a corresponding light neutral particle called neutrino. While the electron was known for a long time, the existence of the other generations, as well as the presence of different neutrino flavors are relatively recent discoveries. Leptons only participate in weak and electromagnetic interactions. They are often found in a free state as standalone particles.

Quarks are also fermions, but unlike leptons they also participate in strong interactions. Quarks have a fractional charge, and each generation is represented by one particle of charge -1/3 and another one of +2/3. Quarks combine into hadrons of two types: mesons (bosonic particles consisting of quark and anti-quark pair, $q\bar{q}$) and baryons (fermionic particles consisting of three quarks, qqq or $\bar{q}\bar{q}\bar{q}$), although more exotic states such as tetra- and pentaquarks may also exist under special circumstances. The most stable hadrons are those consisting of the lightest quarks - up (u) and down (d), while the most massive top quark (t) is never found inside hadrons, as it decays long before coming into the interaction with other particles.

The gauge bosons are the force carriers of fundamental interactions: photons of electromagnetism, W and Z bosons of the weak interactions, while gluons are the carriers of the strong interactions. The last missing element of the SM was the Higgs boson, discovered in 2012, which proved the Higgs mechanism, that describes how bosons acquire their mass [2,3].

1.2   Quantum Chromodynamics

The theory describing strong interactions is Quantum Chromodynamics (QCD), which associates an additional quantum number called color charge with the quarks and gluons. There are a total of three color charges: red, green and blue, named after the RGB color palette. Anti-particles also come in three different color charges: anti-red, anti-green, and anti-blue. A property of the strong interaction is color confinement: all the free particles must be color-neutral. The composition of hadrons from colored quarks and gluons is shown in Fig. 2. Because of the color confinement, quarks and gluons were discovered much later than their existence was predicted, when deep inelastic scattering experiments at the Stanford Linear Accelerator Center (SLAC) in 1968 confirmed the presence of smaller particles inside protons [4]. These particles, named partons, can be identified with quarks and gluons in high momentum-transfer reactions.
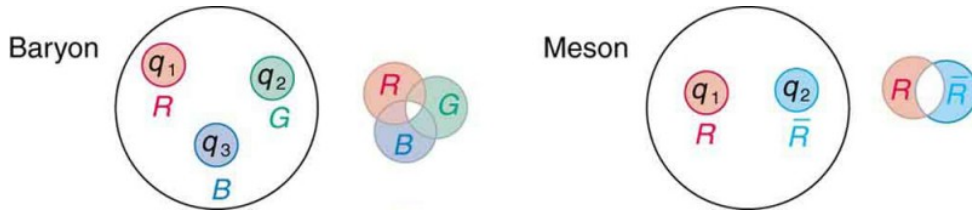
Figure 2: Confinement of colored quarks inside baryons and mesons.

The color confinement effect is caused by the self-interaction of gluons inside hadrons. Colored gluons cause an anti-screening effect, which causes the effective coupling of strong interaction to rapidly increase with distance between color charges, and therefore energy for separation becomes bigger and bigger (see Fig. 3). On the other hand, in reactions with a large momentum exchange the coupling constant is small, and particles move freely. This is called the asymptotic freedom.
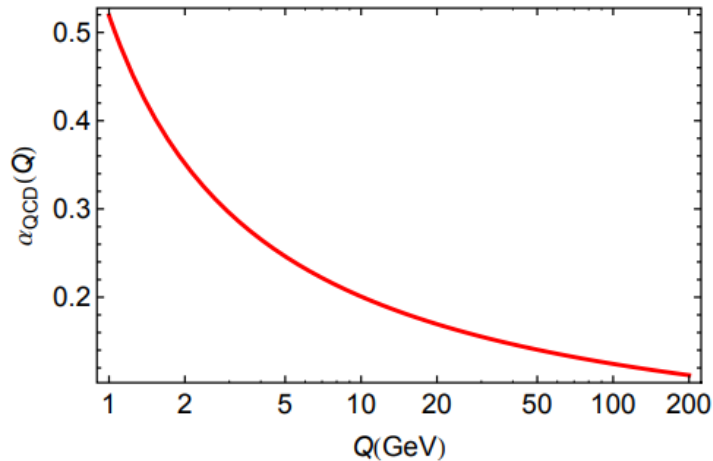
Figure 3: The running coupling constant of the strong interaction in function of the momentum transfer scale Q [5].

If an energetic parton is created in a reaction, it cannot remain in a colored state. Instead, multiple quark-antiquark pairs are polarized out of the vacuum, which form hadrons afterwards. This process is called the fragmentation, and results in a collimated spray of hadrons that can be associated to a high-momentum initiating parton. Such a shower is called a jet (Fig. 4). As $q\bar{q} \rightarrow q\bar{q}$ and $qq \rightarrow qq$ processes are the most common in QCD high-momentum scatterings, jets are often found emerging back-to-back in the so-called dijet structures.

It has been long predicted by theoretical works that the state of matter in which quarks and gluons can be found in an unconfined state should exist [6]. Such a medium,

3

called Quark-Gluon Plasma (QGP), can only exist at an extremely high temperature and density. Finding the QGP and measuring its phase diagram became possible with modern particle accelerators, which perform particle collisions at very high energies.

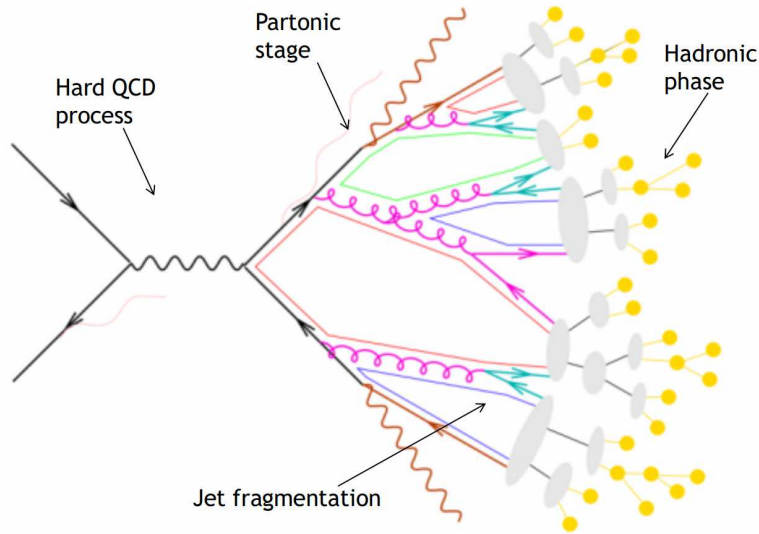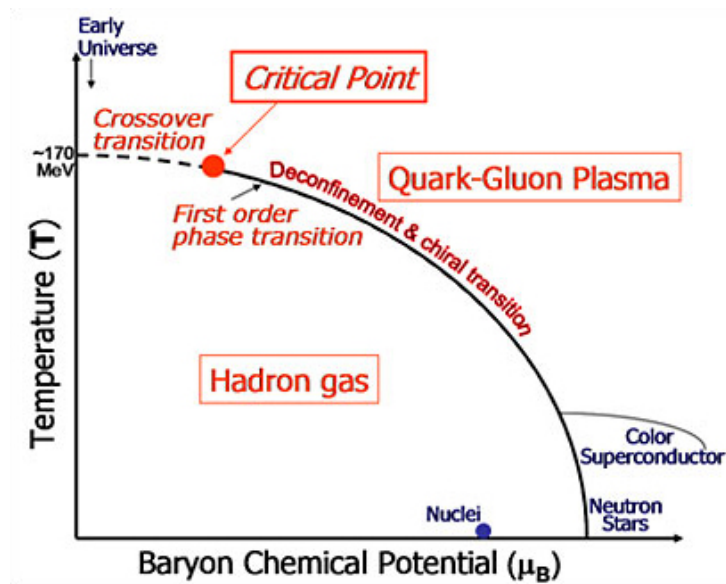**Figure 4:** Particle jet formation process [7].

Figure 5: Phase diagram of the QGP [8]. There is a crossover transition between the QGP state and the hadron gas beyond the critical point.

1.3 Discovery of the Quark-Gluon Plasma

Although promising signatures of the QGP were already seen at the Super Proton Synchrotron (SPS) at CERN, clear evidences were provided by the Relativistic Heavy

Ion Collider (RHIC) experiments in the early 2000s [9]. The STAR experiment at RHIC analyzed the dijet structures of particles in proton-proton (pp), deuteron-gold (d–Au), and gold-gold (Au–Au) collisions [10]. Angular correlation of particles within the leading jet (near-side peak, at a relative angle around $\Delta\phi = 0$) were observed in pp, d–Au and Au–Au collisions. However, while the correlations of the leading jet with the subleading jet can be seen in pp and d–Au collisions (away-side peak, at $|\Delta\phi| \approx \pi$), and also in peripheral Au–Au collisions, it is completely absent in central (highly overlapping) Au–Au collisions, as seen in Fig. 6. This proved the presence of a strongly interacting medium in central Au–Au collisions that is neither present in d–Au nor in peripheral Au–Au collisions, and the secondary jet lost most of its energy during the interaction with it. This process is called the jet quenching [11].
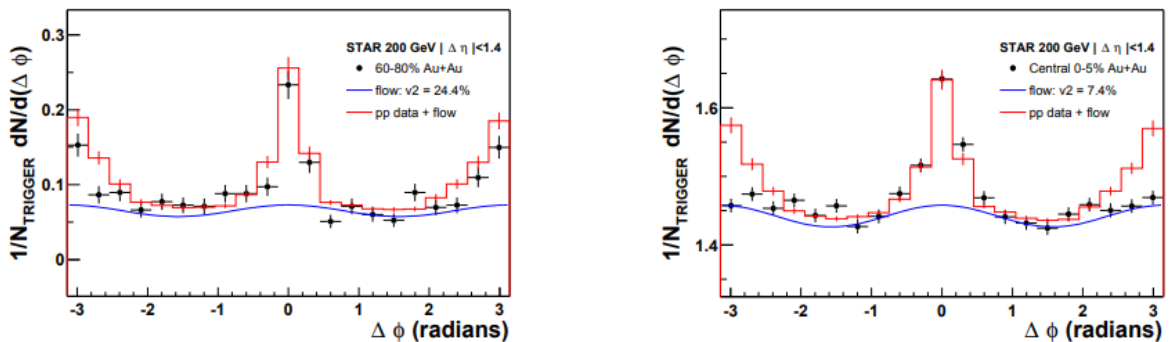

Figure 6: Azimuthal correlation of particles in peripheral and central Au–Au collisions at STAR experiment compared to pp collisions at $\sqrt{s_{\mathrm{NN}}}$=200 GeV [12].

If in heavy-ion collisions a hot and dense medium is created, it is expected to emit thermal radiation. Measurements at the PHENIX experiment showed an excess of direct photons in the thermal regime, that implies an initial temperature in the range of 300-600 MeV in Au–Au collisions at $\sqrt{s_{\mathrm{NN}}}$=200 GeV, which corresponds to approximately 2-4 trillion K [13]. As the phase transition of it is predicted to be at the temperature around 170 MeV, this proved, that particles created in a collision are in the state of QGP. In central lead-on-lead (Pb–Pb) collisions at $\sqrt{s_{\mathrm{NN}}}$=2.76 TeV at the LHC, the initial temperature can be estimated to be a slightly higher, 385-740 MeV [14].

In theoretical works it had been assumed that the QGP contains quarks and gluons in the state of asymptotic freedom, and therefore the QGP would behave like ideal gas. Experiments, however, showed that the QGP exhibits a strong coupling and behaves like an almost perfect (non-viscous) fluid. In non-central heavy-ion collisions, the bulk matter

is created with spatial anisotropy, in a rougly almond-shaped volume (see Fig. 7). Because of the strong coupling, pressure builds up and drives particles away from the interaction point. Pressure will be the highest in the reaction plane (the plane determined by the two beam axes), where the matter has been compressed more strongly. Thus the original spatial anizotropy translates to a momentum anizotropy. This is usually expressed in the terms of Fourier expansion in the azimuthal angle [15]. A sizeable second Fourier-coefficient (v_2 or the elliptic flow) is present in RHIC $\sqrt{s_{NN}}$=200 GeV Au–Au collisions as well as in Pb–Pb collisions at $\sqrt{s_{NN}}$=2.76 TeV at the LHC [16,17]. The v_2 at RHIC is shown in Fig. 8a.
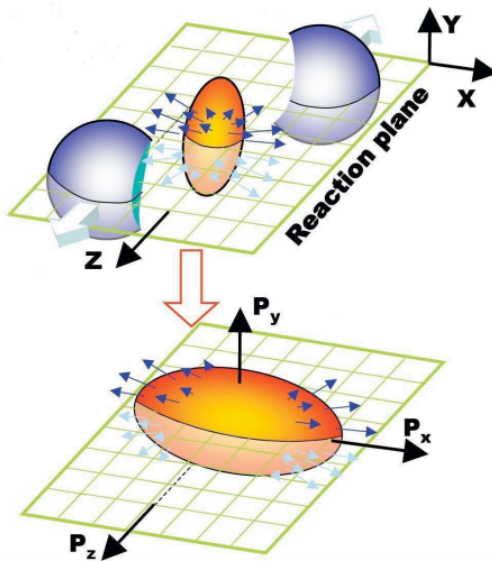

Figure 7: Creation of elliptical shaped "fireball" in non-central heavy ion collision.

If the flow is expressed in terms of the transverse kinetic energy KE_T, an almost perfect scaling with constituent quark number can be observed between different hadron species at RHIC energies [18] (Fig. 8c). This means that the collective behavior stems from a phase where the primary degrees of freedom are quarks.

1.4 Collectivity in proton-proton collisions

Collectivity also manifests in long-range two-particle correlations. Measurements of particle correlations in small collision systems of proton-lead (p–Pb) and pp were performed at CMS experiment [19,20]. Surprisingly, a pattern emerged in events that have a high final-state multiplicity, that is very similar to the one observed in Pb–Pb colli-
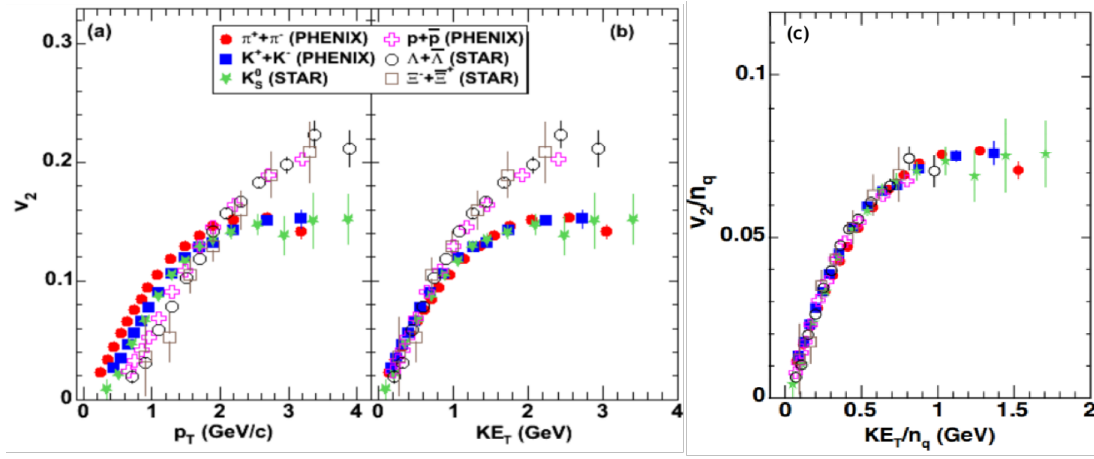
Figure 8: (a) v_2 vs transverse momentum p_T, (b) v_2 vs transverse kinetic energy KE_T, (c) v_2 vs transverse kinetic energy scaled by the number of constituent quarks (n_q=2 for mesons and 3 for baryons) for identified particle species obtained in minimum bias Au–Au collisions [18].

sions (Fig. 9). Besides the correlation near $\Delta\phi = 0$ relative angle, which is caused by the correlation of particles from the same jet, a broad correlation region at $\Delta\phi \approx \pi$ in total pseudorapidity coverage was also observed. In Pb–Pb collisions this phenomenon can be understood with the presence of QGP, but it is still an open question whether the QGP can cause this collective behaviour in smaller collision systems, as the center-of-mass energy of these collisions is not sufficient to produce the QGP in significant volumes.
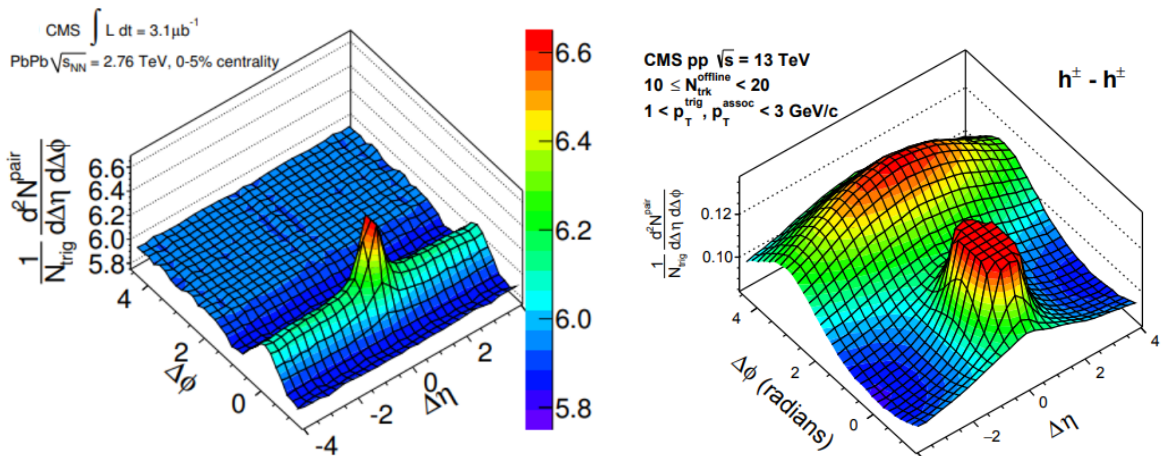
(a) Correlation between particle pairs in Pb–Pb collisions [21].

(b) Two-particle correlation in high-multiplicity pp system [20].

Figure 9

7

However, the presence of the QGP is not necessary to explain collectivity in small systems, as relatively soft vacuum-QCD effects can also produce a similar behaviour. One of these effects is the Multiple-Parton Interaction (MPI) processes [22]. A schematic drawing of a pp collision with MPI is shown in Fig. 10.
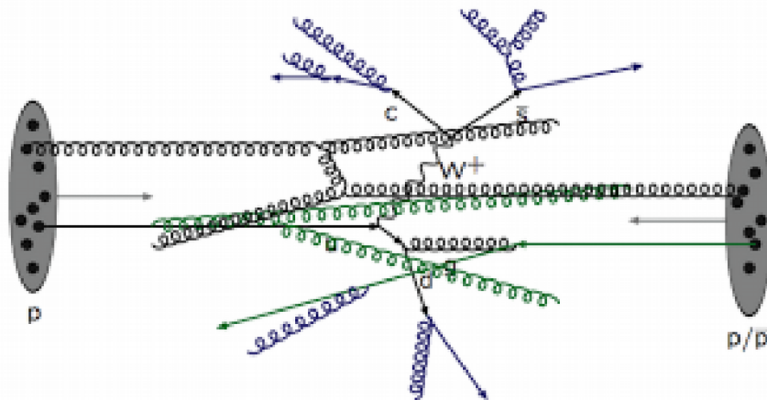
Figure 10: Schematics of the Multiple-Parton Interaction [23].

There are two major forms of MPI. First, multiple partons within the projectile and target hadron can scatter, causing more than one hard processes. And second, partons can rescatter on each other [24]. Multiple parton interactions increase overall multiplicity by enhancing the production of underlying event (UE), or mostly soft hadrons that are not directly related to the leading hard process.

Multiple parton interactions are also expected to depend on the flavor of the emerging particles. Fragmentation of heavy-flavor jets is expected to differ from light-flavor jets because of color charge and mass effects. The internal structures of heavy-flavor jets may therefore provide a deeper insight into the flavor-dependent development of jets and their connection to the UE.

1.5   Role of heavy flavor in high energy collisions

The charm (c) and beauty (b) quarks are produced in the early stages of the collisions. Their mean lifetime is sufficient to survive throughout the collision, hadronize and escape the interacting medium, while bringing information about every stage in the collision. Therefore their detection can give us insight into the processes happening in the collision. By using probes with heavy flavor in collisions of heavy nuclei we can gain information on the QGP, while detecting them in pp collisions may help better understand the nature

of collectivity in small collision systems.

The lightest heavy flavor particles are D mesons. They contain a c quark bound to a light or strange (s) antiquark (or the other way round). The only possible decay for them is a weak decay of the c quark into one of the lighter u or d quarks, meaning that D mesons mostly decay into pions and kaons. The D mesons are not detected directly as their mean life time, though much longer than the timescale of the collision, is not long enough to reach the detectors. However, modern detectors already have a good enough precision for measuring the secondary vertex of their decays, which helps with reconstructing the original mesons from their decay products. The lifetime of the D mesons, $\tau_{\mathrm{D}}c$ (where c is the speed of light) varies between 100-300 μm, B mesons have a lifetime $\tau_{\mathrm{B}}c$ of around 400-500 μm, while the secondary vertex resolution is in the range of 100 μm.

B mesons contain a b (anti)quark, as well as one of the u, d, s, or c (anti)quark, which means that they often decay into mesons with charm quark components – D mesons. This makes detecting them an even more complicated task, because even their primary decay products are not always detected directly. Also, they contribute to the production of D mesons, which can influence D-measurements. This so-called feed-down contribution is excluded from prompt D meson measurements that aim to understand charm physics.

In my thesis I summarize a measurement of transverse event activity (R_{T}) dependent D^0 meson production that I performed in the ALICE experiment. I detail the experimental methods, as well as some important variables in Chapter 2. In Chapter 3 I present the main steps of the measurement of an R_{T}-integrated analysis, then in Chapter 4 I discuss the steps specific for the R_{T}-differential measurement. Finally, before I conclude, I present my results from the current status of the analysis in Chapter 5.

2 Experimental methods

2.1 The LHC and the ALICE experiment

The Large Hadron Collider at CERN is the world's largest and most powerful particle accelerator. The LHC consists of a 27-kilometre ring of superconducting magnets with a number of accelerating structures to boost the energy of the particles along the way. There are a total of 4 experiments at the LHC: ATLAS, CMS, LHCb and ALICE. While ATLAS and CMS use general-purpose detectors to investigate broad range of physics, ALICE and LHCb rather focus on more specialized studies.

A Large Ion Collider Experiment (ALICE) is optimized for studying heavy ion collisions (mostly Pb–Pb), as well as smaller systems of p–Pb and pp collisions. ALICE focuses on the physics of strongly interacting matter at extreme energy densities. The main subject of study at the experiment is the primordial state of matter – the QGP and its evolution. This allows for the investigation of the nature of strong interactions and color confinement. Recent studies also concentrate on small collision systems with high final-state multiplicity, where QCD mechanisms on the soft-hard boundary that lead to collective behaviour can be explored.
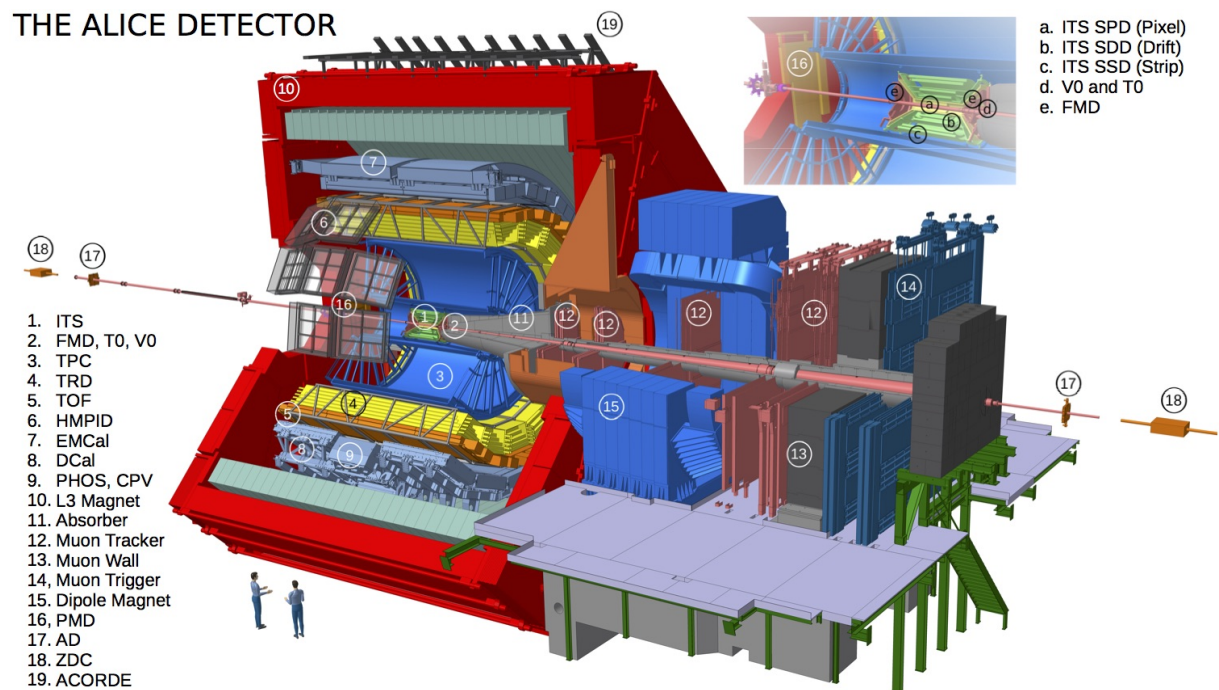
Figure 11: The ALICE experiment with denoted detector systems. A detailed description of the detector is presented in [25]

ALICE consists of 18 detector subsystems, each serving a different task in identifying particles emerging from the collision, and measuring their properties. Mainly the data from Inner Tracking System (ITS) and Time Projection Chamber (TPC) was used in my studies. The ITS consists of six cylindrical layers of silicon detectors. Their purpose is to identify the spatial origin of a particle, which penetrates them, with very high precision (up to the fractions of a milimeter). This enables us to determine whether the particle originated from the initial collision in the primary vertex, or is a product of a weak particle decay at a secondary vertex. The TPC is an 88 m^3 volume gas detector, and it is the main particle tracking device in ALICE. Charged particles moving through the gas medium ionize it, freeing electrons that drift towards the end plates of the detector. The characteristics of the ionization process caused by fast charged particles passing through a medium can be used for particle identification.

2.2 Kinematic description of high energy collisions

In ultra-relativistic collisions a set of kinematic variables is used for better convenience. As inelastic scattering processes can be characterized by the momentum transfer perpendicular to the beam axis, often the projection of the total momentum of the particles on the transverse plane is used, the transverse momentum p_T.

Another variable, used for measuring the deviation of particles from the beam axis is the pseudorapidity η. It is calculated from the polar angle θ between the total momentum of the particle and the positive direction of the beam line:

$$\eta = -\ln\left(\tan\frac{\theta}{2}\right) \tag{1}$$
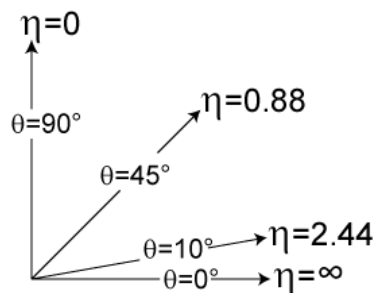
Figure 12: Correspondence between pseudorapidity values and the poalr angle θ between momentum of the particle and the positive direction of the beam line.

11

The rapidity, which is usually used in the realtivistic physics, is estimated as follows:

$$y = \frac{1}{2} \ln \frac{E + p_z c}{E - p_z c} \qquad (2)$$

where E is the energy of particle, while p_z is its momentum component along the particle beam axis.

The advantage of pseudorapidity over the rapidity is that it is purely geometrical, with direct connection to the polar angle. However, in the limit of $m \to 0$ (or $E \approx |\vec{p}|$) the values of rapidity and pseudorapidity are close: $y \approx \eta$.

To describe the energy of the pp collision a square root of the Mandelstam variable s is used, as it is a Lorentz-invariant quantity. The value of $\sqrt{s}$ represents the centre-of-mass energy of the colliding beams.

2.3   Charged particle multiplicity

Charged particle multiplicity is one of the basic observables in collider experiments, giving information about both soft and hard QCD processes happening during the collision. Studying of multiplicity distributions can give us insight into the particle production and the UE activity.

The multiplicity of an event can be defined in different ways, depending on the object of study. Technically the most simple multiplicity estimator is the number of particles at mid-rapidity. However, a drawback is that this multiplicity will include the jet corresponding to the hard process under investigation, therefore auto-correlations can bias the results. A remedy to this, in case of a suitable detector, is to introduce a rapidity gap between the acceptance of the measurement and that of the multiplicity estimation.

In the measurement of multiplicity in pp collisions presented in [26] two different methods are used for the multiplicity estimation:

- Measuring the number of tracks in the pseudorapidity region $|\eta|<0.8$ (mid-rapidity multiplicity)

- Measuring the total charge deposited in the forward detector covering the pseudo-rapidity regions $2.8<\eta<5.1$ and $-3.7<\eta<-1.7$ (forward multiplicity).

The transverse momentum dependence on the mid-rapidity multiplicity can be seen in Fig. 13a. A stronger than linear dependence of average p_T is observed (as shown in

Fig. 14), which may indicate the presence of autocorrelation processes. This is expected, as both the multiplicity and transverse momentum are estimated in the same region.

To minimize the autocorrelation effect the forward multiplicity estimator was used, the result is presented in Fig. 13b. In this case the transverse momentum dependence on multiplicity is closer to linear, which confirms the possible bias with the previously used multiplicity estimator.

(a) Mid-rapidity multiplicity.

(b) Forward multiplicity.
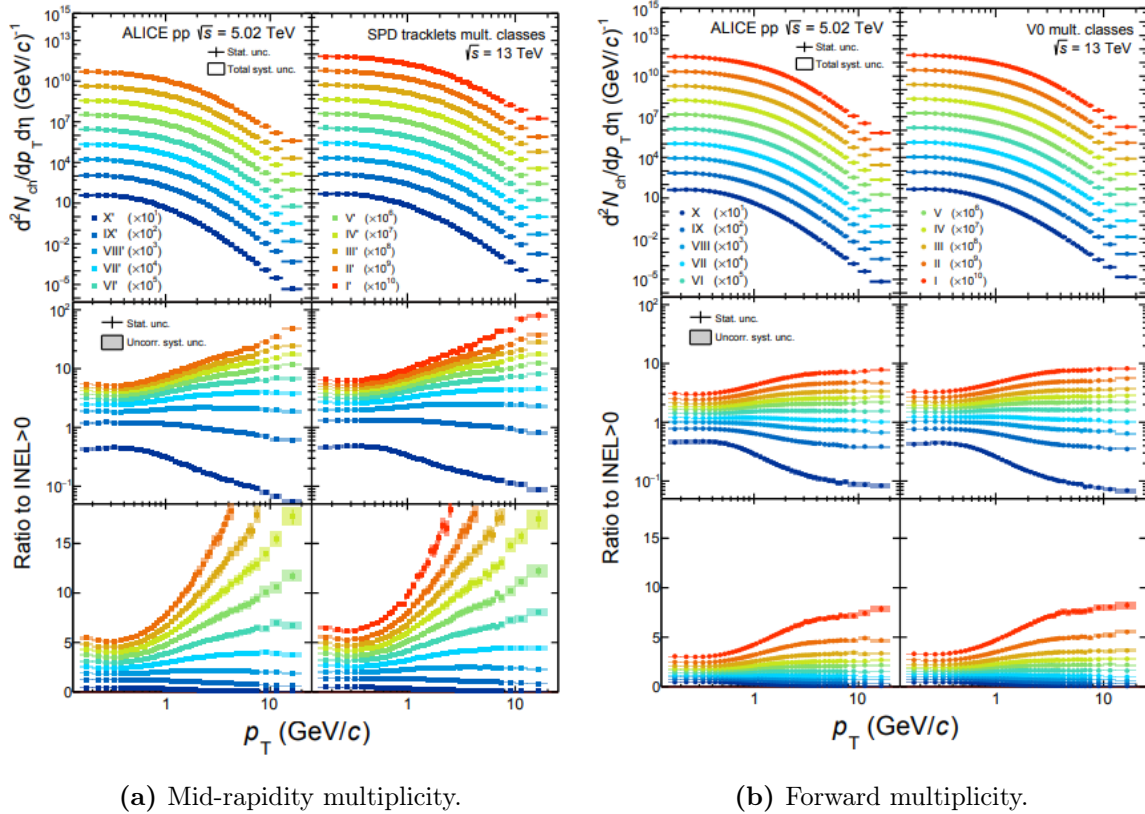
Figure 13: Transverse momentum dependence on the mid-rapidiry and forward multiplicity. Different colours represent different multiplicity regions (red - the lowest multiplicity, dark blue - the highest) [26].

2.4   The transverse multiplicity

Jet production is associated with the hard processes in the collision. As my goal is to study the production of heavy-flavor particles, the correlation effects between multiplicity and jets need to be excluded. A possibility to achieve this at mid-rapidity is to estimate the multiplicity in regions, where jets are not present. The transverse plane of a collision can be divided into three regions of equal area with respect to the leading particle (particle with highest p_T momentum) in the event:
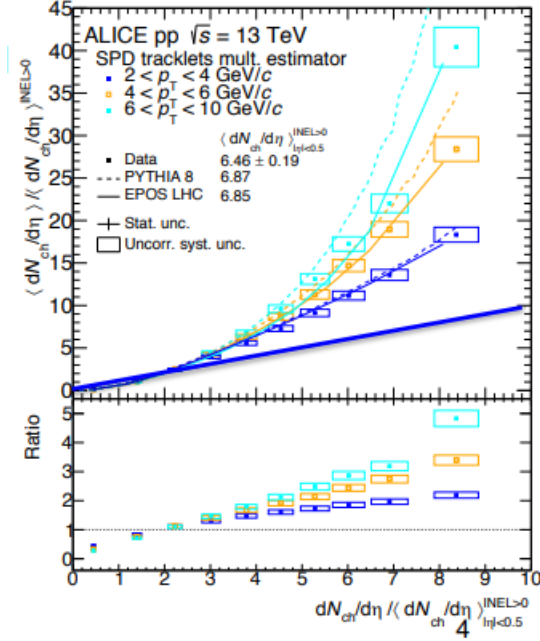
Figure 14: Self-normalized particle production as function of multiplicity [26].

- $-\frac{\pi}{3} < \Delta\phi < \frac{\pi}{3}$: Forward region - this area contains most of the fragments of the jet that contains the leading particle.

- $\frac{2\pi}{3} < \Delta\phi < \frac{4\pi}{3}$: Away region - particles from the recoil jets in back-to-back processes will show up mostly in this area.

- $\frac{\pi}{3} < \Delta\phi < \frac{2\pi}{3}$ and $-\frac{2\pi}{3} < \Delta\phi < -\frac{\pi}{3}$: Transverse region - contains the underlying events. Jet fragments from the primary hard process are strongly suppressed in this region.

Here $\Delta\phi = \phi - \phi_{\text{lead}}$ is the difference between the leading particle and a given particle in azimuthal angle. This definition is represented in Fig. 15.

Multiplicity is then taken on the transverse side, and is expressed in terms of the so-called transverse event activity classifier R_{T}, which represents the self-normalised charged-particle multiplicity in the transverse region only:

$$R_{\text{T}} = \frac{N_{\text{trans}}}{\langle N_{\text{trans}} \rangle}, \tag{3}$$

where N_{trans} is the charged particle number in transverse region and $\langle N_{\text{trans}} \rangle$ is its average in all events. According to simulations, R_{T} is strongly correlated to MPI in a collision [27], therefore measuring it will indirectly classify events by MPI.

14
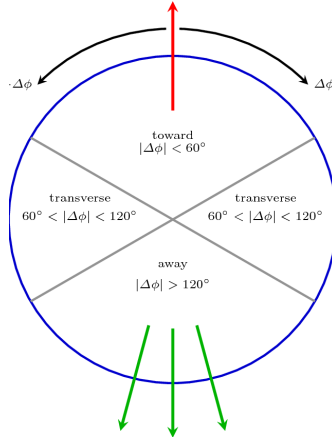
Figure 15: Definition of toward, away and transverse region in the transverse plane.

If one measures the dependence of the average particle production in different regions as function of the transverse momentum of leading particle, then an interesting effect can be observed (see Fig. 16). When the leading particle has low transverse momentum, particle production in all the regions rises similarly. However, for events with leading particles having $p_{\mathrm{T}}^{\mathrm{leading}} > 5 \, \mathrm{GeV}/c$, the difference between transverse region and two other regions is observed. The particle production in transverse region barely changes creating a so-called jet plateau, meaning, that particle production in the transverse region is almost independent from the hard processes happening during the collision.
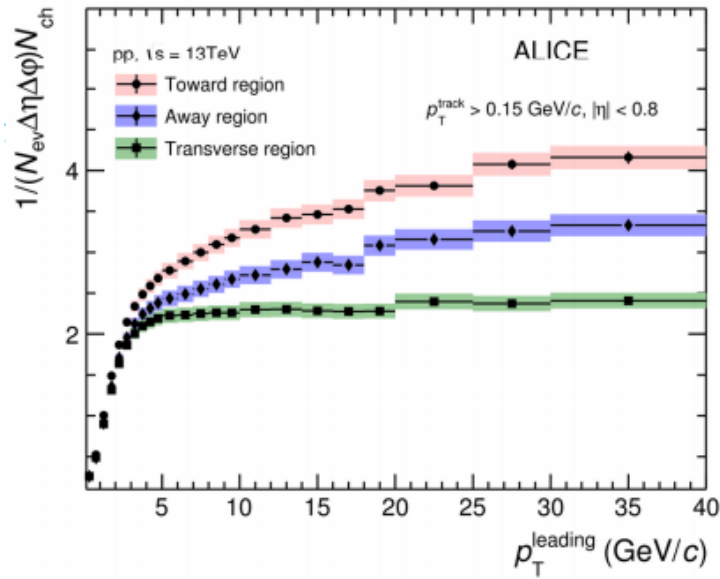

Figure 16: The average particle production in different regions in function of the $p_{\mathrm{T}}^{\mathrm{leading}}$ [28].

An analysis was performed in ALICE to investigate the particle production using the transverse activity classifier [29]. The self-normalised charged particle yields as a function of R_T are shown in Fig. 17. Because of autocorrelation, one can expect a stronger-than-linear dependance in the transverse region, which is actually the case. Also, particle production in the toward region shows weaker dependence on the transverse activity classifier R_T. Also note that a substantial hard particle production is present on the toward side even when the transverse activity is very low, giving an opportunity to study jets with almost no UE activity.
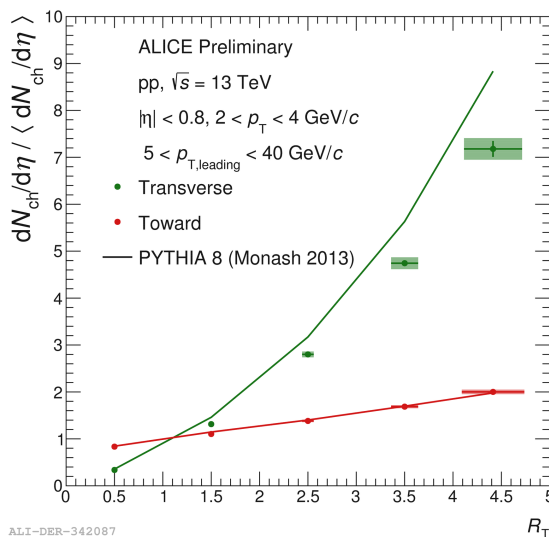
Figure 17: Self-normalized charged particle yields in function of transverse activity classifier R_T.

Fig. 18 shows an ALICE measurement of R_T-differential charged-particle spectra in pp collisions at $\sqrt{s}$=13 TeV [30]. Different trends are observed in the toward and transverse regions. In the toward region the spectra corresponding to lower-than-average transverse activity ($R_T<1$) is harder than the spectra corresponding to higher-than-average transverse activity ($R_T>1$). In the transverse region an opposite behaviour is present. One can conclude that an almost complete separation between the soft (UE) and hard jet parts of the event was achieved at high p_T. Moreover, the auto-correlation effects are significantly reduced [31].
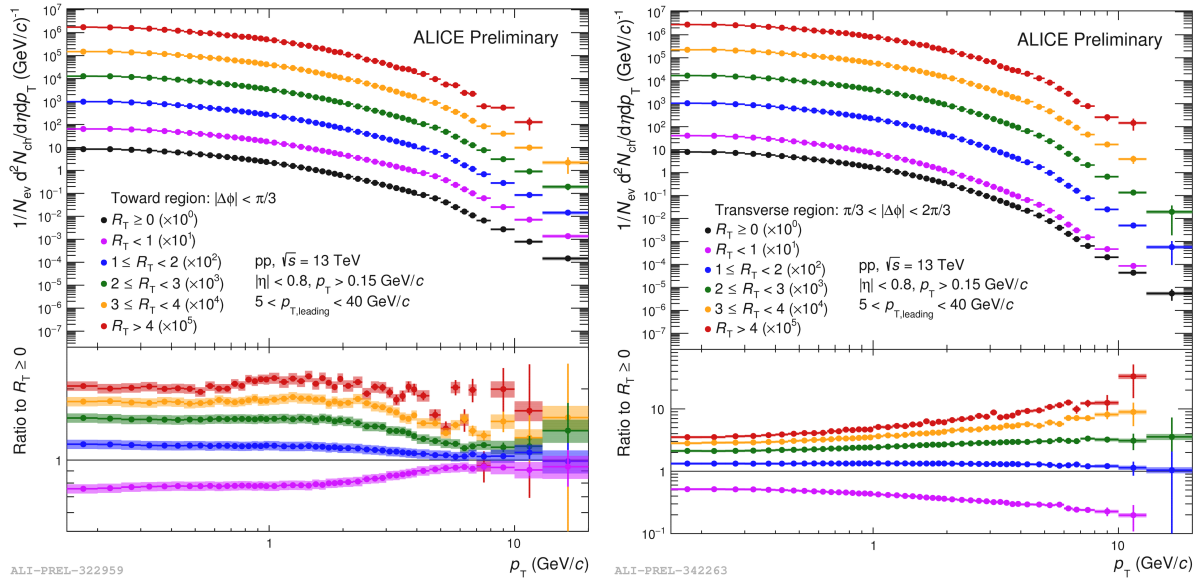
(a) Toward region.　　　　　**(b)** Transverse region.

Figure 18: Transverse momentum spectra of charged particles in R_T bins [30].

2.5　Probing the underlying event with heavy flavor

Heavy flavor can be utilized to investigate the influence of the different semi-hard and soft processes on their production. Such a phenomenology study was performed using PYTHIA Monte-Carlo event generator [32,33]. PYTHIA 8 [34] simulates the hard processes with leading order QCD calculations, that are followed by a partly phenomenological modelling of initial-state radiation, multiple-parton interactions and final-state radiation on the partonic level. Afterwards, fragmentation is applied using the Lund string model, and as a last step it calculates the decays of the unstable particles to obtain the final state. Since the conservation of color charge is not guaranteed in the partonic-level calculations, a mechanism called color reconnection (CR) is applied in conjunction with the MPI processes.

The influence of the MPI and CR on light and heavy flavor production was studied in toward and transverse regions of a reaction plane. To demonstrate the effect of these components in the simulation, PYTHIA was run with CR switched on and off. In each case, the leading particles were identified, and the number of π, p, D or the B mesons $(N_{\pi,p,D,B}(p_T^{lead})$) were recorded in function of their momenta. Afterwards, the ratios to the pion numbers were taken $(N_{p,B,D}(p_T^{lead})/N_\pi(p_T^{lead})$). Finally, a double ratio between

17

the CR on and off cases were taken:

$$K_{\mathrm{p,D,B}}^{\mathrm{CR}}(p_{\mathrm{T}}^{\mathrm{lead}}) = \frac{N_{\mathrm{p,B,D}}(p_{\mathrm{T}}^{\mathrm{lead}})/N_{\pi}(p_{\mathrm{T}}^{\mathrm{lead}})|_{\mathrm{CR=off}}}{N_{\mathrm{p,B,D}}(p_{\mathrm{T}}^{\mathrm{lead}})/N_{\pi}(p_{\mathrm{T}}^{\mathrm{lead}})|_{\mathrm{CR=on}}} \tag{4}$$

The same was repeated with MPI on and off, while the CR was switched off.

In the case of color reconnection being switched on and off (Fig. 19) a separation between heavy and light flavor is observed. While the ratios between pions and protons are close to unity, there is a clear separation according to flavor, as the relative production of D mesons decreases if CR is on, and B decreases even more. However, there is barely any difference between processes happening in the toward and transverse regions. This indicates that the color reconnection is sensitive to the flavor, but not the mass of the leading particle, and it acts similarly regardless of the relative location from the leading hard process.
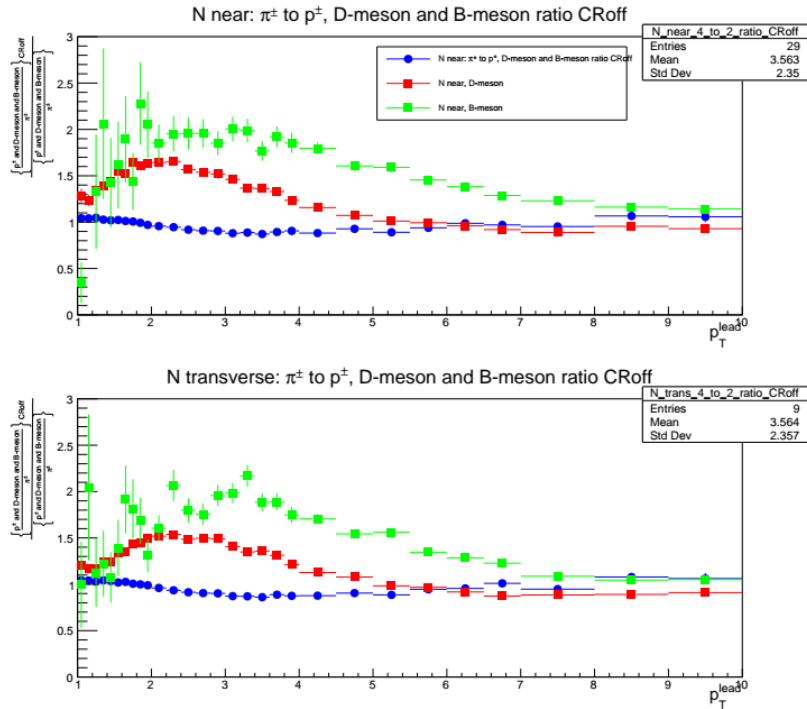
Figure 19: Double ratios in events with CR switched off and on shown in the toward region (upper) and the transverse region (lower). Blue markers represent pions, red markers - D mesons, and green markers - B mesons [32].

Considering the events with MPI processes being included or excluded from the calculations (Fig. 20) a similar flavor ordering is observed in the toward region, however the presence of MPI now causes increase in heavy flavor production. But a totally different

behaviour is present in the transverse region. While the ratios of pions and protons are similar, there is also no difference between D and B except for the low-p_T part. There is one split between heavy and light flavors. This indicates that the jet structure is sensitive to the flavor, most likely via the dead-cone effect, the underlying event is determined by the color charge (ie. that a large fraction of the light jets are from gluons, while heavy-flavor jets are quark-initiated).
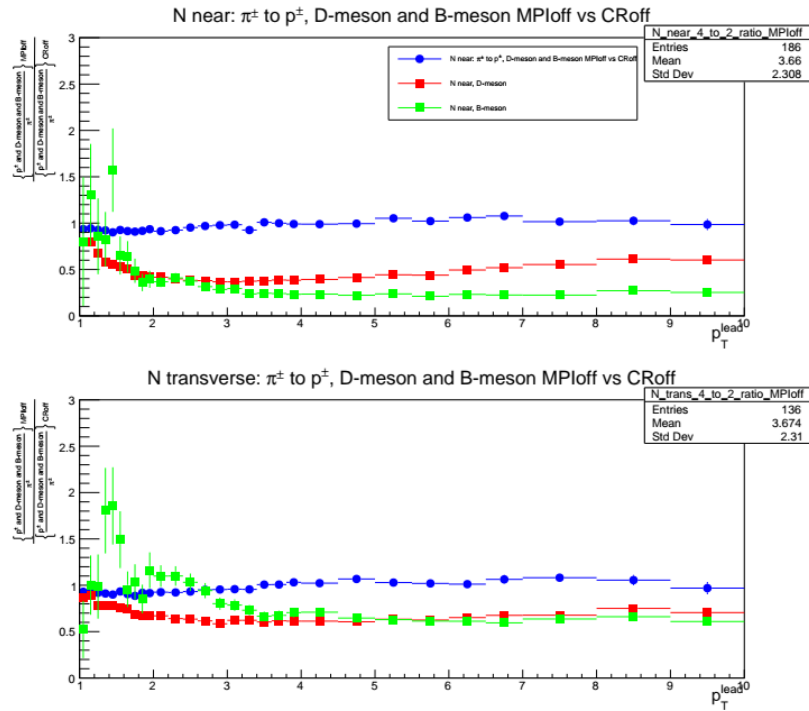
Figure 20: Double ratios in events with MPI switched off and on shown in the toward region (upper) and the transverse region (lower). Blue markers represent pions, red markers - D mesons, and green markers - B mesons [32].

3 Measurement of azimuth-integrated D^0 meson production in pp collisions

The aim of this thesis is to outline an analysis of D^0 production in function of the transverse event activity R_T. However, before the R_T-dependent analysis I performed a measurement of azimuth-integrated D^0 meson production to test my analysis method and demonstrate the feasibility of the upcoming study. Although I concentrate on the D^0, a similar analysis is possible and will be carried out in ALICE with other non-strange D meson species (D^+, D^{*+}). There are differences in the reconstruction and selection of D mesons, however, the remaining analysis steps are similar. In the next chapters both the D^0 meson ($c\bar{u}$) and its antiparticle, $\overline{D^0}$ ($\bar{c}u$), are referred to as D^0.

3.1 Datasets and event selection

For the analysis I used data collected by the ALICE experiment during the LHC Run-II in period of 2016-2018 years for the proton-proton collisions at $\sqrt{s}$=13 TeV center-of-mass energy. For the Monte Carlo simulations PYTHIA events embedded into real-data underlying events were used. To simulate the detection of particles in PYTHIA events the GEANT3 detector simulation package was used [35].

The same event selection process was used as described in [36]. To reject background events stemming from the interaction of beam particles with the beam pipe materials or beam-gas interactions, only events with interaction vertex in the range $|z|$<10 cm were used for the analysis. The vertex reconstruction is performed in two ways simultaneously: by analyzing data from the Silicon Pixel Detector (SPD), and by the reconstruction of the particle tracks. In case where the primary vertex could be reconstructed with both SPD and tracks, the two z-positions are requested to be compatible, otherwise one of the events is rejected as a pile-up event. When the two vertices are found to be too close in z-direction, no pile-up rejection is applied since it becomes very difficult to distinguish between a real pile-up event and a fake one.

3.2 D^0 meson reconstruction

D^0 mesons which originate in the primary vertex, never reach detectors due to their very short mean lifetime: $\tau_{D^0} = (410.1 \pm 1.5) \times 10^{-15}$ s [37]. Thus, it is not possible to detect the D^0 mesons directly, so instead the daughter particles of the meson's decay have to be detected and identified. In the ALICE experiment the decay channels, which are used for D^0 identification are

$$D^0 \rightarrow K^- + \pi^+$$
$$\overline{D^0} \rightarrow K^+ + \pi^-$$

The reason why these processes are used is that they are the only hadronic decays in which all the daughter particles are non-neutral with sufficiently high branching ratio (i.e. probability with which the decay happens), which is equal to $\mathrm{BR}_{D^0 \rightarrow K^- \pi^+} = 3.89 \pm 0.05\%$ for the D^0 decay process [37].

In ALICE charged kaons and pions are identified with the TPC detector by measuring their specific energy loss $\frac{dE}{dx}$ inside the detector volume. The performance of the TPC is shown in Fig. 21. The curves corresponding to the different particle species follow the Bethe-Bloch formula. As can be seen, differentiation between particle species is especially pronounced at low momentum, while at higher momenta the regions corresponding to the species start to overlap, and particle identification is no longer unambiguous. In my analysis the 3σ compatibility cut was applied to the difference between the measured and expected signals for the particle in the p_T-dependent normalized distributions.

Through different topological selections one can exclude those pion-kaon pairs that are not likely to have originated from the same D^0 decay. The schematics of the process can be seen in Fig. 22. The tracks of kaon and pion are extrapolated back to their origin and beyond. This way the impact parameters and distances of closest approach (DCA) can be determined. The DCA is defined as the smallest distance at which kaon and pion pass one another. This point is close to the secondary vertex, which is not reconstructed in this analysis. The momentum of the reconstructed D^0 meson is determined as the sum of momenta of kaon and pion. The angle between the flight line of D^0 meson and the direction of the momentum D^0 candidate is called a pointing angle, θ_point.

To determine whether a kaon-pion pair originated from the same decay process a set of topological cuts has to be applied. These set up an allowed range for each of the kinematics
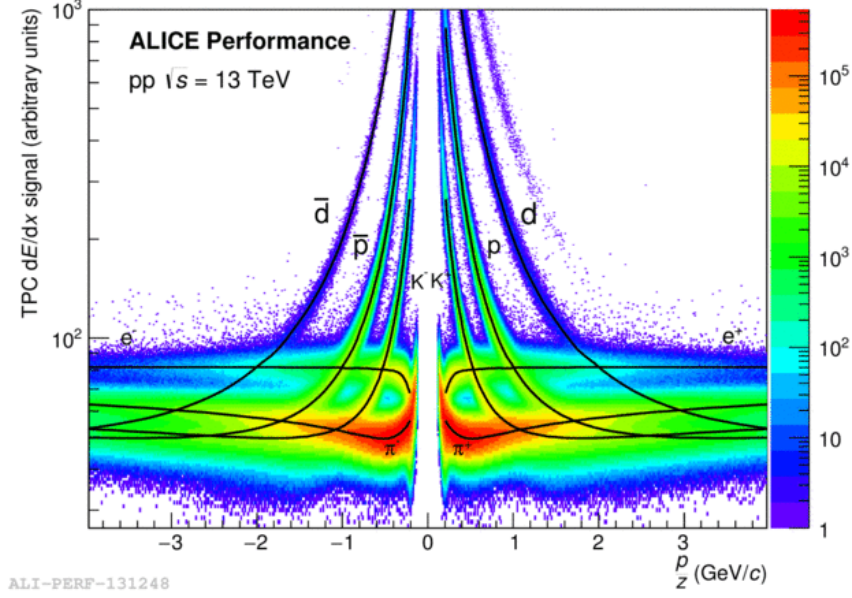
Figure 21: The Energy Loss measurement performance as a function of the momentum in the TPC detector at $\sqrt{s}$=7 TeV [38].
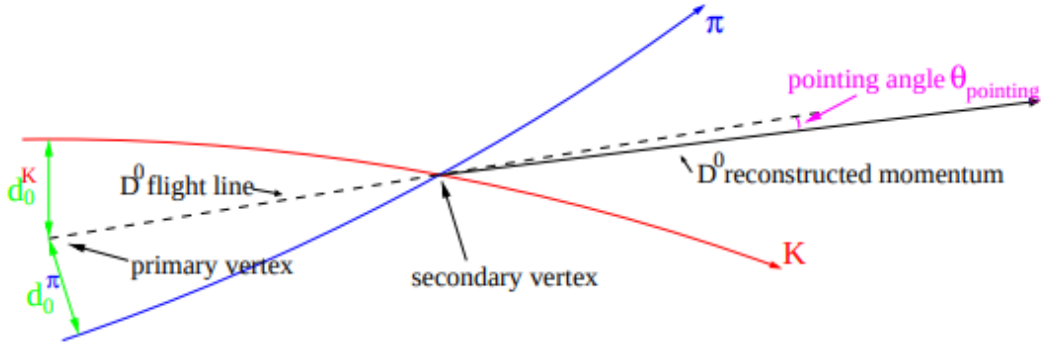
Figure 22: The schematics of the D^0 decay into a charged pion and kaon pair. The black dashed line shows the trajectory of the D^0 meson originated in the primary vertex. This line is extrapolated to the right beyond the location of the decay (the secondary vertex). The black arrow represents the momentum of reconstructed D^0 meson. The blue and the red arrows represent the reconstructed tracks of pion and kaon respectively, while the green arrows show their impact parameters [39].

variables described below. There are a total of six such parameters:

- $|M_{D^0} - M_{rec}|$ - the difference between the rest mass of the D^0 (M_{D^0} = 1864.84 MeV/c^2 [37]) and the mass of reconstructed D^0 meson. Candidates with too large mass differences will be excluded, as they are very unlikely to represent a true D^0.

22

- DCA - the distance of closest approach between the daughter particles. If kaon-pion pair originated from the same decay, then their reconstructed tracks are expected to come close enough at some point (which is near the secondary vertex).

- p_T^K and p_T^π - transverse momenta of the kaon and the pion identified in the TPC. As we look for the decay products of a heavy particle, their momenta is expected to be at least 0.3 GeV/c.

- $|d_0^K|$, $|d_0^\pi|$ and $d_0^K d_0^\pi$ - impact parameter of kaon and pion, and their product. These variables express how close a D^0 track gets to the primary vertex. The negative values of $d_0 d_0$ (see table 1.) are due to the tracks that pass the primary vertex on different sides.

- $\cos\theta^*$ - the cosine of the initial flight line direction of the D^0 in the center-of-mass frame of the collision. To decrease the combinatorial background, events from the regions with high suppression of D^0 production are excluded.

- $\cos\theta_{\text{point}}$ - the cosine of the pointing angle. The D^0 candidate is required to move in a similar direction to the supposed original meson.

All the cuts are defined differently for every transverse momentum interval. The applied value ranges for some p_T intervals can be seen in Table 1.

The next step in the analysis after finding the D^0 candidates is to apply the topological cuts for every collision event. Altogether, out of more than 9 billion analyzed events approximately 12 million candidates were accepted.

3.3 Invariant mass distribution of D^0 candidates

After the reconstruction, all D^0 meson candidates are grouped according to their transverse momentum p_T into 12 intervals of 1-2, 2-3, 3-4, 4-5, 5-6, 6-7, 7-8, 8-10, 10-12, 12-16, 16-24 and 24-36 GeV/c. After this, for each reconstructed D^0 meson its invariant mass is calculated as

$$M_{\text{inv}} = \sqrt{(E_{\text{K}} + E_\pi)^2 - (\vec{p_{\text{K}}} + \vec{p_\pi})^2} \tag{5}$$

where E_{K} and E_π are the energies of kaon and pion, $\vec{p_{\text{K}}}$ and $\vec{p_\pi}$ are the three-momenta of kaon and pion. The natural units are used with c equal to 1. While most of the false

Cuts	p_T interval (GeV/c)			
	1-2	4-5	8-9	12-16
$|M_{D^0} - M_{rec}|$ (GeV)	<0.4	<0.4	<0.4	<0.4
DCA (μm)	<300	<300	<300	<300
p_T^K (GeV/c)	>0.4	>0.7	>0.7	>0.7
p_T^{π} (GeV/c)	>0.4	>0.7	>0.7	>0.7
$|d_0^K|$ (μm)	<1000	<1000	<1000	<1000
$|d_0^{\pi}|$ (μm)	<1000	<1000	<1000	<1000
$d_0 d_0$ (μm^2)	<-25000	<-8000	<-5000	<10000
$\cos\theta^*$	<0.8	<0.8	<0.9	<1.0
$\cos\theta_{point}$	>0.8	>0.85	>0.85	>0.85

Table 1: Applied topological cuts in some of the transverse momentum intervals.

candidates from randomly associated kaon-pion pairs are rejected by the topological cuts, there are still many that accidentally pass them. In order to account for this so-called combinatorial background, all the candidates are filled into histograms of invariant mass. One of these histograms can be seen in Fig. 23a, where the invariant mass distribution of D^0 meson candidates having transverse momentum in the range 4-5 GeV/c is shown. Histograms for other p_T intervals have a similar shape, as presented later in Fig. 24.

On each histogram one can clearly see a peak around the true D^0 rest mass. There is a combinatorial background under the peak from randomly paired pions and kaons that pass the topological cut. The drop in the number of candidates that can be seen at invariant mass above 2.1 GeV/c^2 is because of kinematical restrictions imposed by the topological cuts, and it is outside the mass window used in the analysis.

By fitting the histogram with combination of exponential function for background, and Gaussian for the mass peak (Fig. 23b), a position of the peak (*mean* value) and a standard deviation (*width* value) can be obtained. For the fitting a χ^2 distribution was used. In the interval of three standard deviations (1.5σ to both sides from the mean value) a *Signal*(S) and *Background*(B) values can be calculated. The background value B is calculated as the integral of the fitted exponential function in the beforementioned 3σ window. There are two methods for obtaining the signal value S:

24

(a) The invariant mass distribution of the reconstructed D^0 candidates.
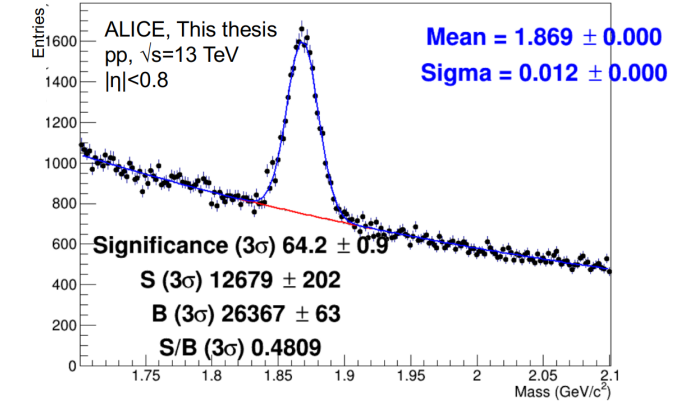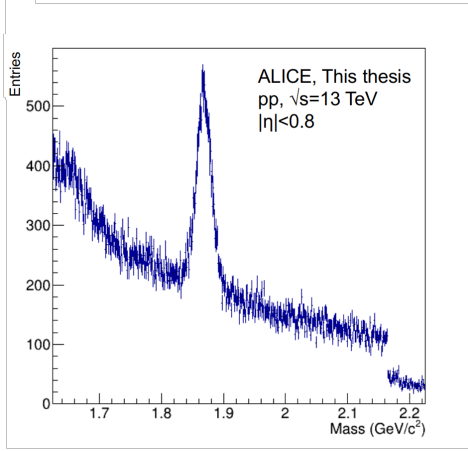
(b) Fitting of the invariant mass distribution of the reconstructed D^0 candidates. The blue curve is the fitted Gaussian function with parameters shown in the upper right corner. The red curve is a fit of background with the exponential function.

Figure 23: The invariant mass distribution of D^0 candidates after topological selection.

- calculate the integral of the Gaussian fit in the range of 3σ

- calculate the integral of the data (ie. perform bin counting) and subtract the integral of fitted exponential function in the range of 3σ

The relative difference between two methods is in the range of 5% and for further calculations the first method was used. Using the signal and background values the significance Σ of the signal can be determined:

$$\Sigma = \frac{S}{\sqrt{S + B}} \qquad (6)$$

The signal extraction was performed in all p_T intervals. All the twelve histograms can be seen in Fig. 24. A few observations can be made based on them:

- D^0 meson candidates with low transverse momentum (p_T<3 GeV/c) have relatively low significance, because of the low S/B ratio.

- Low significance can also be seen for candidates having high transverse momentum (p_T>10 GeV/c). Here the explanation is that altogether there are much less data, so signal itself is small.

25

- The fit function describes well the invariant mass distributions in all p_T regions, with χ^2/ndf values in the range 1–1.4.
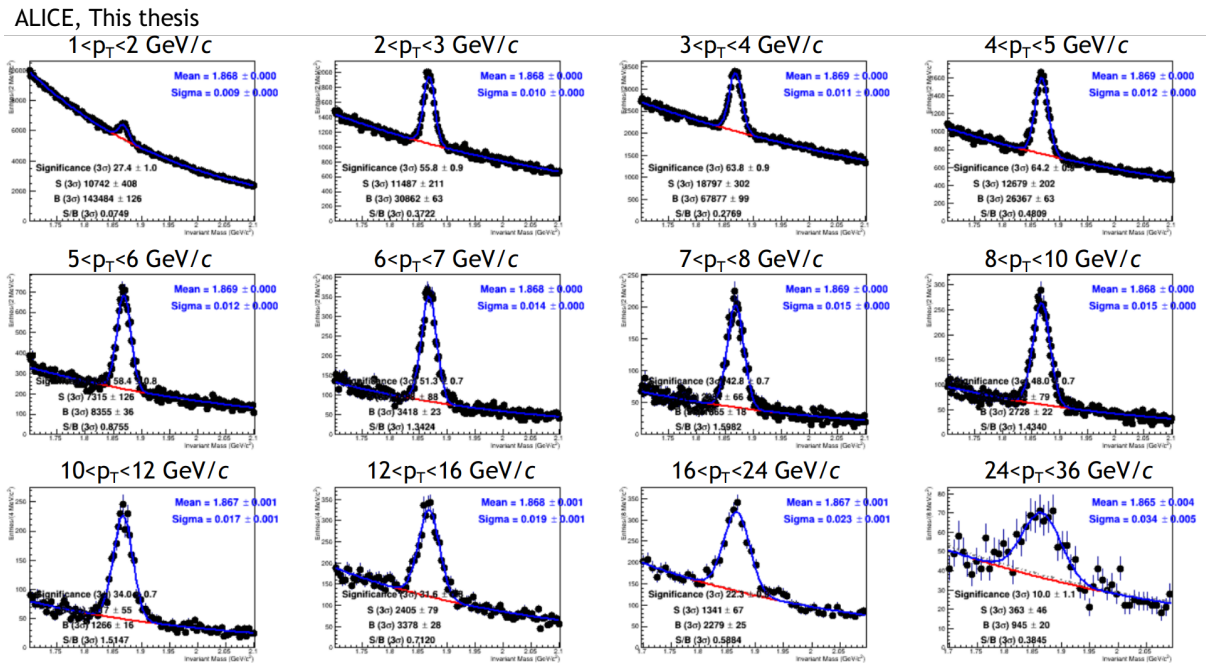

Figure 24: Invariant mass distribution of the D^0 candidates in all p_T regions with fitted functions, the fitted means and widths as well as the signal and background counts.

The extracted values for the means and widths are summarized as a function of p_T and are shown as blue markers in Fig. 25. The invariant mass of reconstructed D^0 mesons is very close to the rest mass of this hadron, the biggest deviation being around 40 MeV/c^2.

The same analysis procedures were also performed with the Monte Carlo samples. One big advantage of the simulations is that one can surely know which candidates are properly reconstructed D^0 mesons, and which ones belong to the background. In this way the clean D^0 peak can be fitted with a Gaussian and the determination of its parameters is not biased by the background. As a result, the fit parameters provide clean information about the (simulated) reconstruction inaccuracies such as the detector resolution and mass shifts. The parameters of fitted Gaussians for MC simulations are represented with red points in Fig. 25. The two sets of points on the invariant mass graph are not totally consistent. The simulation slightly deviates from data in the case of means at low p_T, and in the case of widths towards high p_T. This can be a result of the background fitting in case of data, as well as of a probable slight mismatch between data and detector simulation.

However, one should note that the discrepancy is in the order of 0.2% at most.
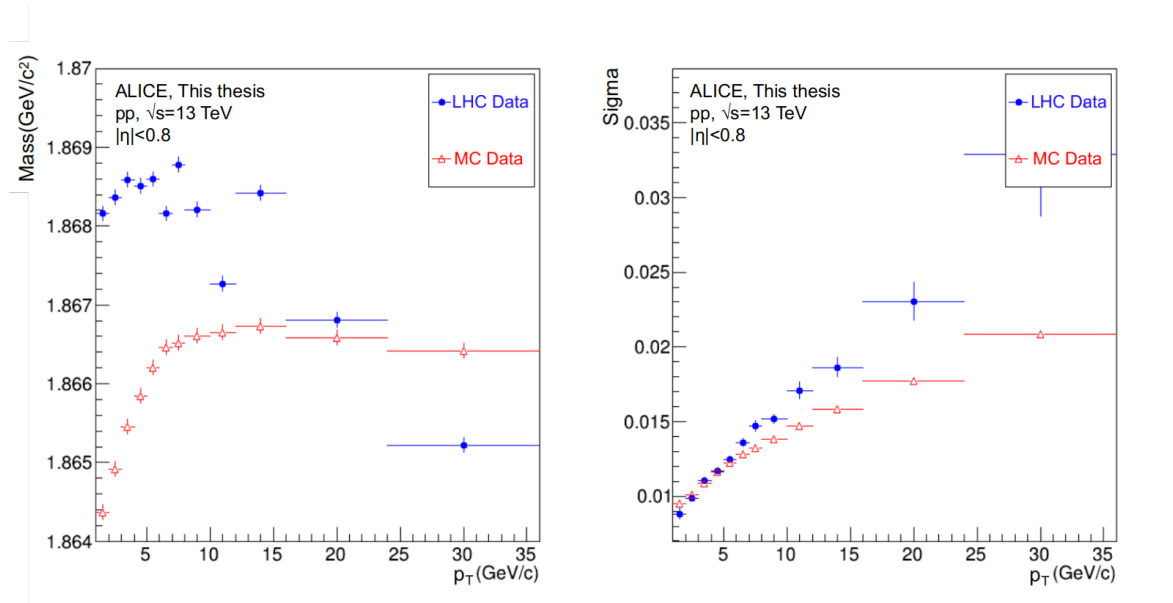
Figure 25: The parameters of the fitted Gaussian functions representing the invariant mass of D^0 candidates and width of the mass peak shown as function of transverse momentum p_T.

3.4   Corrections

Detectors have limitations in their range of operation. Because of this not every particle emerging from the collision is detected. As a consequence, the raw results of measuements do not necessarily represent the underlying physics processes. To get rid of this problem a set of different corrections need to be applied.

The first correction is due to acceptance limitations, which is the geometrical efficiency of a detector. It follows from the fact that the detector does not cover the total 4π solid angle. The acceptance correction Acc depends solely on geometrial factors such as pseudorapidity coverage and radial distance from the primary vertex. The phase space that is designed to correspond reasonably closely to what is experimentally accessible by the detector and reconstruction algorithms is called the fiducial region. Its boundaries are denoted by the fiducial rapidity $|y_{fid}|$. For the combination of TPC and ITS detectors this region is defined as $|y_{fid}| < 0.5$ for particles with transverse momentum below $p_T = 5$ GeV/c, and $|y_{fid}| < 0.8$ for particles having $p_T > 5$ GeV/c. Particles reconstructed outside of the fiducial region are taken to be unreliable, and therefore their contribution

is excluded. Although the pure acceptance correction factor is always below unity, this is not the case when taking the fiducial cut into account. As the transverse momentum of D^0 meson candidates increases, there are more and more of them detected outside of the fiducial region, and with that the acceptance parameter rises to the values above unity, representing the overestimation during the reconstruction process. The acceptance is computed by generating the events with MC simulations. In Fig. 26 the acceptance for the prompt D^0 mesons (those which originate from the primary vertex) is shown in function of p_T in the previously defined intervals. Calculations were performed using both the PYTHIA and FONLL models, and the results are within the uncertainty of one another.
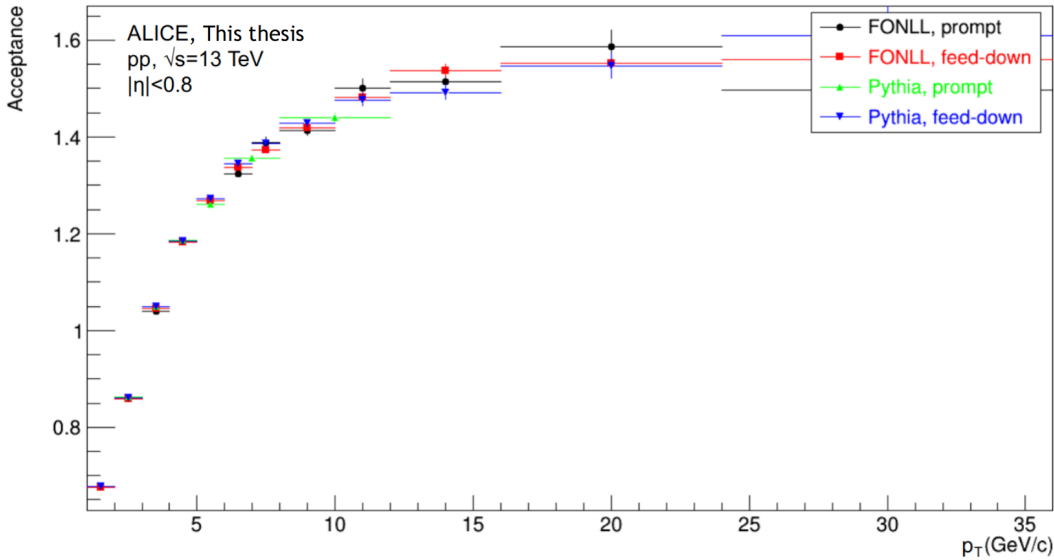
Figure 26: Prompt D^0 and feed-down D^0 acceptance as a function of transverse momentum p_T.

Another detector-related problem is the fact that not all the particles, which reach the detector, are properly detected and identified. The factor which represents this effect is called the efficiency (ϵ) of a detector. Its value is also determined with simulations. Collisions are simulated using MC event generators, and results are then analysed by the same reconstruction chain that was used for the data analysis. As the true identity, as well as the decay chains of all the particles are known in this case, the fraction of successfully reconstructed D^0 mesons can be determined. The results are represented in Fig. 27.

As the acceptance and the efficiency both represent limitations of the detectors, it
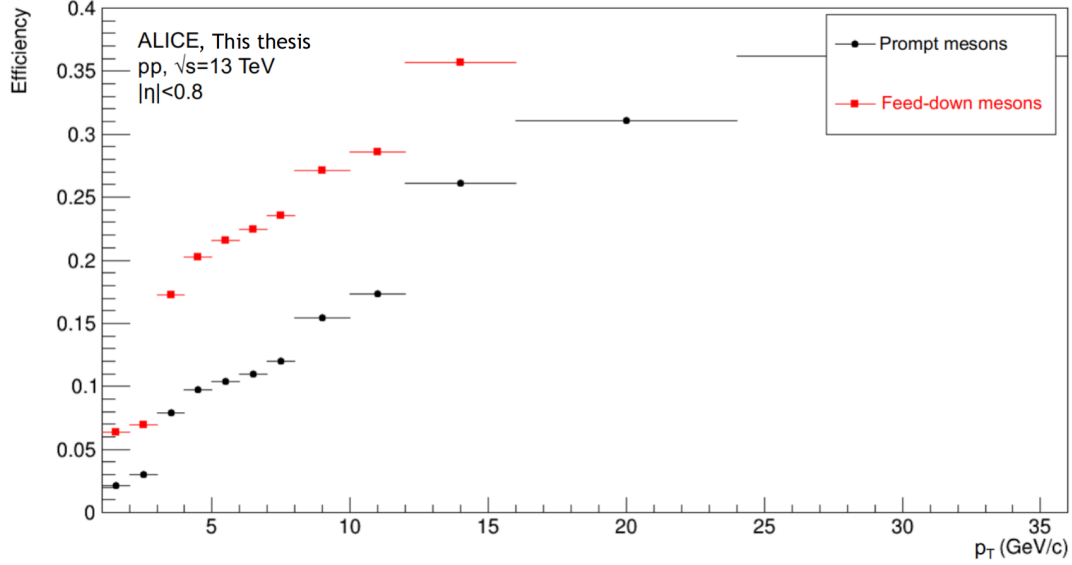
Figure 27: Prompt D^0 and feed-down D^0 efficiency as a function of transverse momentum p_T.

is convenient to use them as a single correction factor. As a result, one can get the acceptance-times-efficiency factor $Acc \times \epsilon$ as a function of transverse momentum p_T representing the properties of detectors. The acceptance-times-efficiency correction factor in function of p_T is presented in Fig. 28.

The Monte Carlo simulation of the events has one more very impotant advantage: by tracing back the ancestry of a D^0 meson we can determine whether it was actually created in the primary vertex, or is a decay product of another long-lived resonance. The feed-down from B to D mesons is schematically represented in Fig. 29. As the goal of this work is to investigate the primordial production of charmed mesons, these mesons need to be excluded from the calculations. To do this, a fraction of prompt D^0 mesons f_{prompt} needs to be calculated as follows:

$$f_{\text{prompt}} = 1 - (\frac{d^2\sigma}{dp_T dy})_{\text{feed-down}} \frac{(Acc \times \epsilon)_{\text{feed-down}}\Delta y \Delta p_T BR \cdot L_{\text{int}}}{N^{D_{\text{raw}}}/2}, \tag{7}$$

where $(\frac{d^2\sigma}{dp_T dy})_{\text{feed-down}}$ is the cross-section of B mesons obtained from FONLL calculations, $(Acc \times \epsilon)_{\text{feed-down}}$ is the acceptance-times-efficiency for the feed-down D^0 mesons (as seen in Fig. 28), Δy and Δp_T are the covered rapidity and transverse momentum regions, BR is the branching ratio of feed-down decay, L_{int} is the integrated luminosity, and $N^{D_{\text{raw}}}$ is the number of raw yields (total number of reconstructed D^0 mesons without any corrections).

29
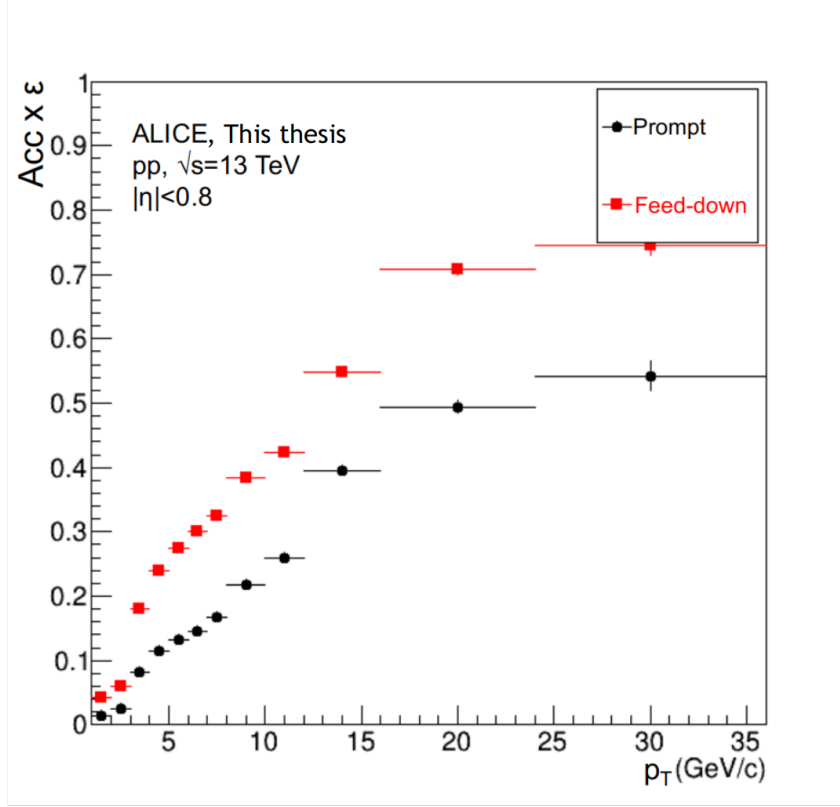
Figure 28: Acceptance-times-efficiency as function of transverse momentum p_T.
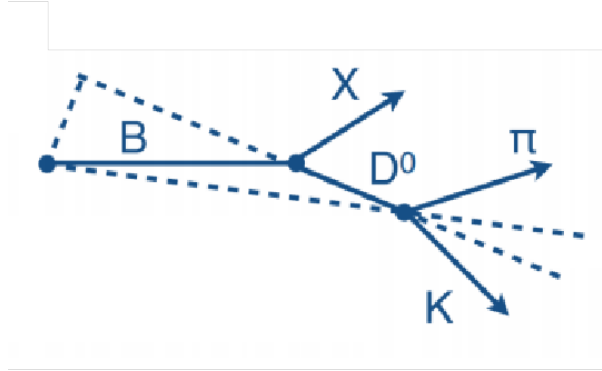
**Figure 29:** Feed-down from B mesons into D^0 mesons.

After considering all of the previous corrections, the cross-section of D^0 meson can be obtained using the formula below:

$$\frac{d\sigma^{D^0}}{dp_T} = \frac{1}{\Delta p_T BR \cdot L_{\text{int}}} \frac{f_{\text{prompt}}(p_T) \cdot \frac{1}{2} N^{D^0_{\text{raw}}}(p_T)}{2y_{\text{fid}}(p_T)(Acc \times \epsilon)_{\text{prompt}}(p_T)}, \tag{8}$$

where $N^{D^0_{\text{raw}}}(p_T)$ is the raw D^0 yield (sum of particles and antiparticles), which is then corrected for the B-meson decay feed-down contribution (i.e. multiplied by the prompt fraction f_{prompt}), divided by the acceptance-times-efficiency for prompt D^0 mesons, $(Acc \times$

$\epsilon)_{\mathrm{prompt}}$, and divided by a factor of 2 to account for the charge-averaging in the raw yield. In order to obtain the production cross-section, the corrected yields also have to be divided by the decay channel branching ratio (BR), the p_{T} interval width (Δp_{T}), the rapidity coverage ($2y_{\mathrm{fid}}$) and the integrated luminosity L_{int}.

In the current state of the analysis, I performed the acceptance-times-efficiency corrections. The corrected yields $\frac{d\mathrm{N}^{\mathrm{D}^0}}{dp_{\mathrm{T}}}$ are shown in Fig. 30. We see that the semi-corrected D^0 yields fall toward higher p_{T} values, as expected. I expect the feed-down correction to slightly modify the yields, however the structure shall remain almost the same.
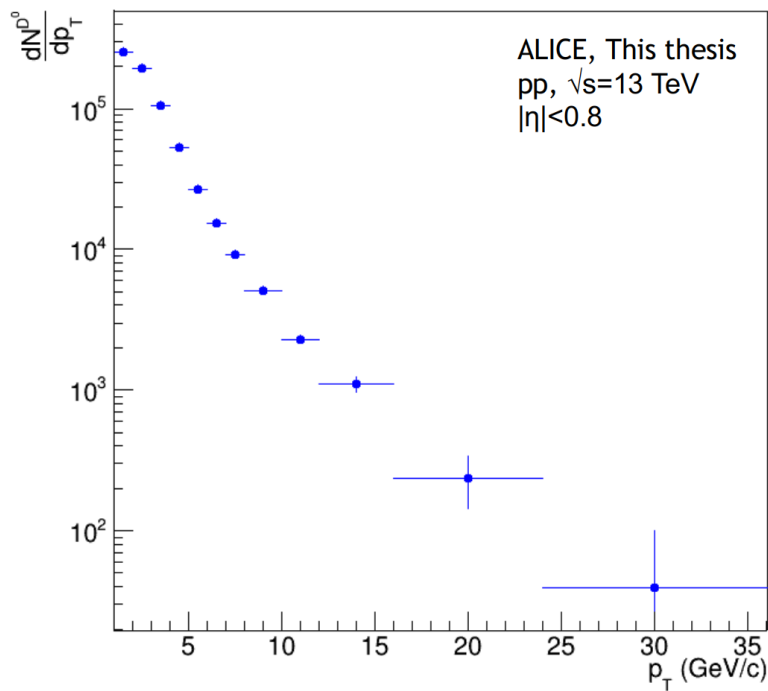
Figure 30: D^0 yields with applied efficiency corrections.

4 D^0 production in dependence of the event activity

4.1 Data quality assurance

During the development of an analysis code, quality assurance (QA) checks are needed to make sure that the data is correctly recorded, processed and interpreted by the analysis code. Basic QA for this dataset was performed in previous analyses [36]. For the D^0 measurement in function of the transverse activity classifier there were two main checks performed: distribution of particles in R_T regions and distribution of the transverse momentum of the leading particle.

The number of particles detected in different R_T regions is shown in Fig. 31. A total of 10 regions were defined in the analysis: 0-1, 1-2, 2-3, 3-4, 4-5, 5-6, 6-7, 7-8, 8-9, 9-10. As the R_T parameter is self-normalized, we expect exactly half of the particles to be detected in the first region. In the performed analysis $8.63 \cdot 10^6$ out of $16.52 \cdot 10^6$ charged particles had been found in the 0-1 R_T region. The cause of the slight discrepancy is that the $< N_\mathrm{trans} >$ was determined on a different dataset.
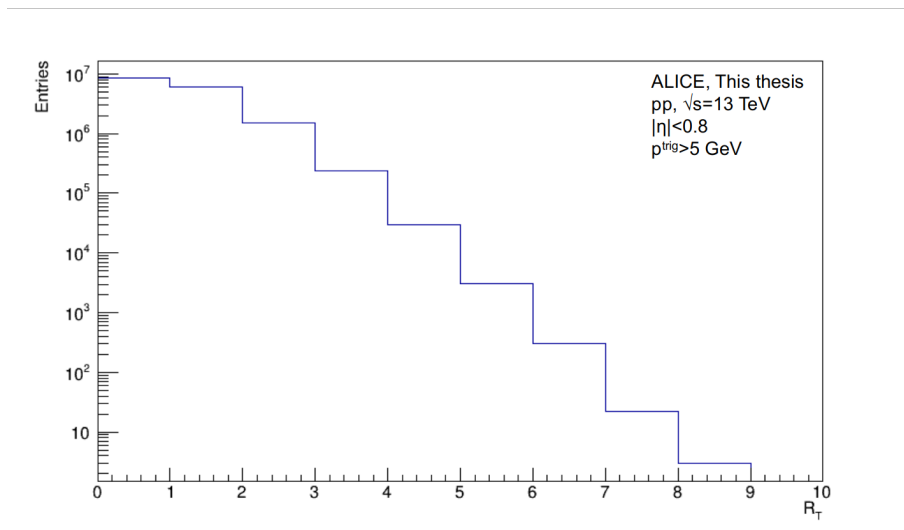
Figure 31: The transverse activity classifier distribution of all the events passing the basic event selection.

The transverse momentum distribution of the leading particle is shown in Fig. 32. A minimum transverse momentum $p_\mathrm{T}^\mathrm{lead} = 5$ GeV/c is required in order to discard events without a high-pT process. After applying this condition, only 1% of total statistics was analyzed.

Most of the heavy-flavor hadrons come in the toward and away regions (see Fig. 15),
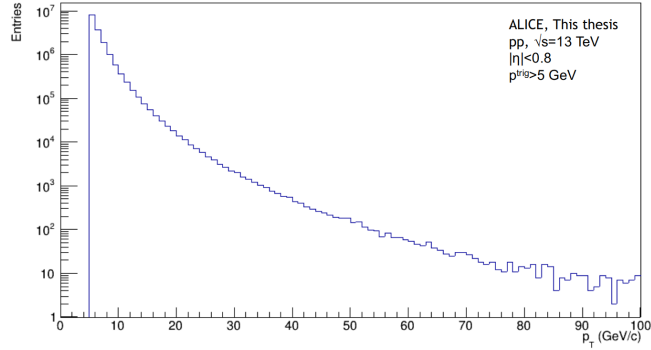
Figure 32: The transverse momentum distribution of the leading particle.

since heavy flavor is mostly created in hard processes and hadronize as part of the leading or subleading jets. To check this, all the D^0 candidates in events with trigger particle having transverse momentum $p_T^{trig} > 5$ GeV/c were grouped by the region where they emerge. The p_T integrated invariant mass distribution of the reconstructed mesons is shown in Fig. 33. Indeed, a clear mass peak is visible in the toward region, while much smaller peak is still distinguishable from the background in the away region. Note that the different D^0 yields at the near-side and away-side peaks is in a large part selection bias: the analysis triggers on a high-p_T hadron in events where there is a D^0, meaning that the leading hadron will be most likely a D^0-decay product, while on the away-side the balancing charm can also follow different (eg. semi-leptonic) decay channels. In the transverse region, however, the D^0 peak is hardly distinguishable from the combinatorial background, indicating that charm production outside the hard jet regions is unlikely.

4.2 Measurement of invariant mass of D^0 mesons in different R_T regions

Considering the distribution of D^0 mesons in R_T intervals, most the statistics falls into the 0-1 and 1-2 intervals, while for the R_T values between 2 and 10 the number of events in each bin falls approximately exponentially. For this reason, in the further analysis the multiplicity intervals of 0-1, 1-2 and 2-10 were used. Also, p_T intervals were redefined to get more even statistics in the intervals: 1-2, 2-3, 3-4, 4-5, 5-6, 6-8, 8-10, 10-12, 12-24 GeV/c. The combinatorial background is not purely exponential if the D^0 candidates are grouped by R_T. For this reason the width of the fitting window was narrowed down. Similarly to the previous chapter, invariant mass distributions for the D^0 mesons were
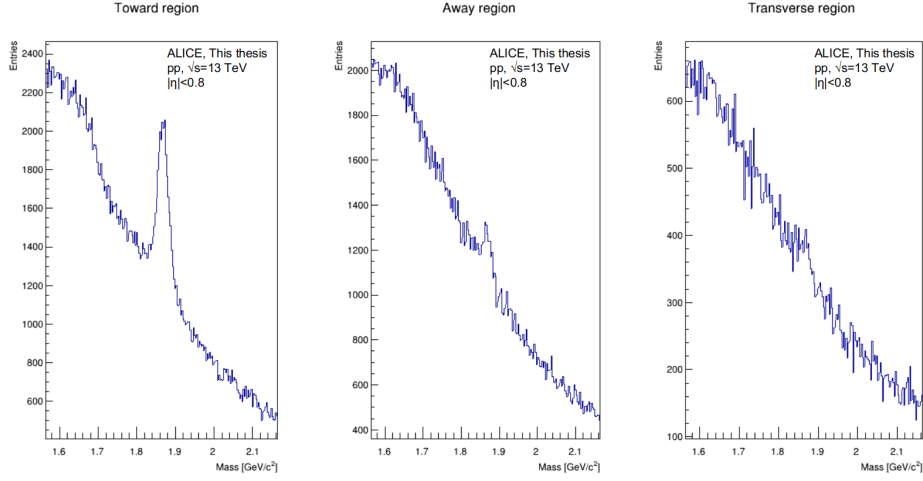
Figure 33: Invariant mass distribution of D^0 mesons detected in toward, away and transverse region.

obtained within each R_T interval. For the sake of brevity, the mass peak plots with the fits are detailed in Appendix A. After fitting the distributions in three azimuthal regions (toward, away and transverse), the mean values for invariant masses of D^0 mesons were obtained, as well as the width of the fitted Gaussians. All the results are presented in Figs. 34, 35 and 36.
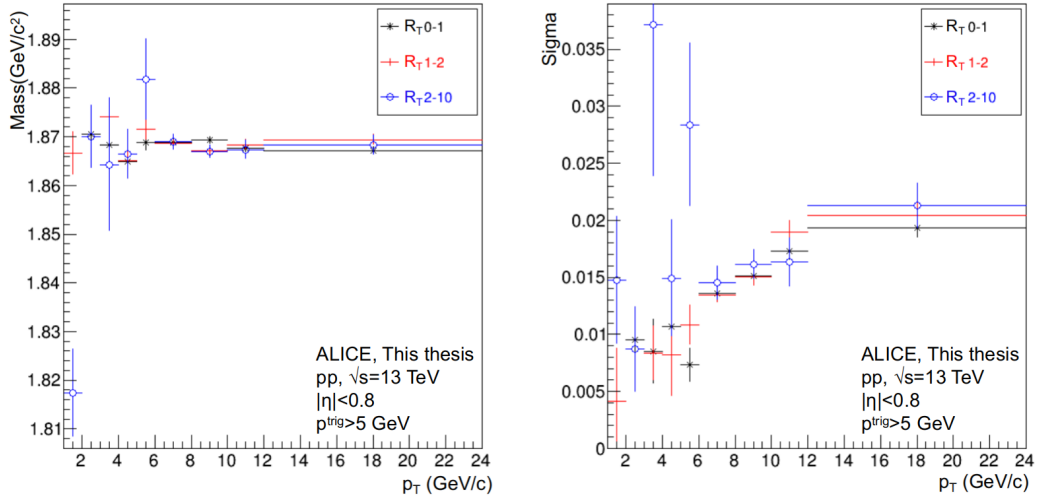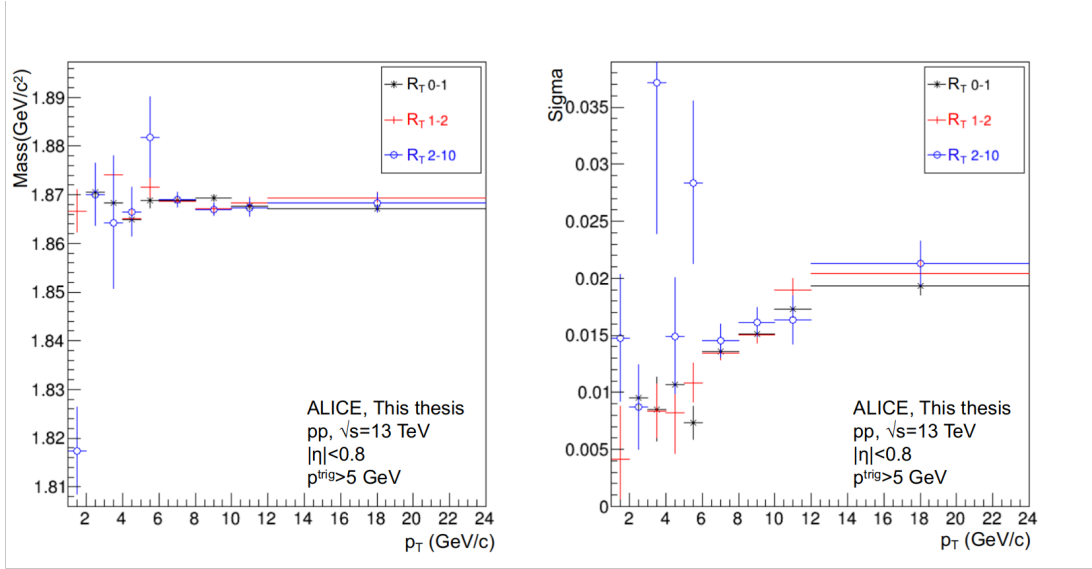

Figure 34: Fitted D^0 invariant mass value in function of p_T in the toward region within different R_T intervals.

All the fitted invariant mass values are close to the rest mass of D^0 meson within uncertainties, even though the uncertainties are bigger compared to the R_T-integrated
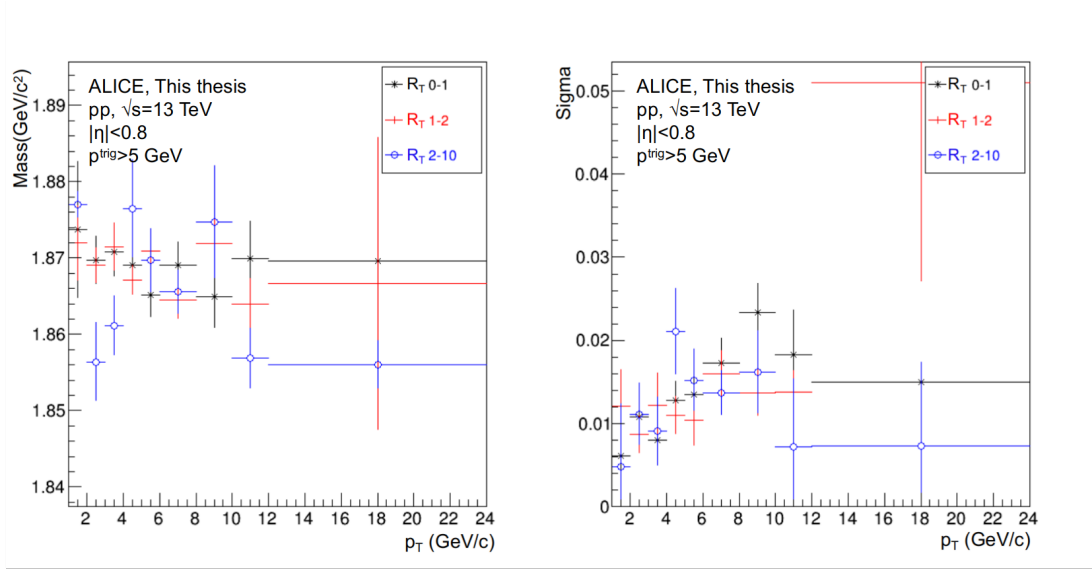
Figure 35: Fitted D^0 invariant mass value in function of p_T in the away region within different R_T intervals.


Figure 36: Fitted D^0 invariant mass value in function of p_T in the transverse region within different R_T intervals.

results. This is a result of lower statistics, especially in the R_T interval of 2-10, and in the transverse region. In some cases the fit was not convergent, these plots are missing from the panels in Appendix A.

5   Results

I used a total of five p_T intervals for the extraction of D^0 yields: 2-4, 4-6, 6-8, 8-12 and 12-24 GeV/c. The D^0 yield is shown in Fig. 37 in each region as function of transverse momentum p_T and the transverse event activity classifier R_T. As mentioned before, there are much less D^0 mesons in the underlying event than in the jet regions. However, D^0 mesons with lower p_T are relatively evenly distributed among the three regions. This is because at low p_T the leading particle might be a deflected decay product of the D^0 mesons, or the leading particle might not be a decay product of a soft D^0 meson at all. However, D^0 mesons with $p_T > 6$ GeV/c are predominantly found in the toward region, while the number of yields in the away and transverse region drops. This indicates that at higher p_T values, the leading particles indeed stem from the D^0 meson.
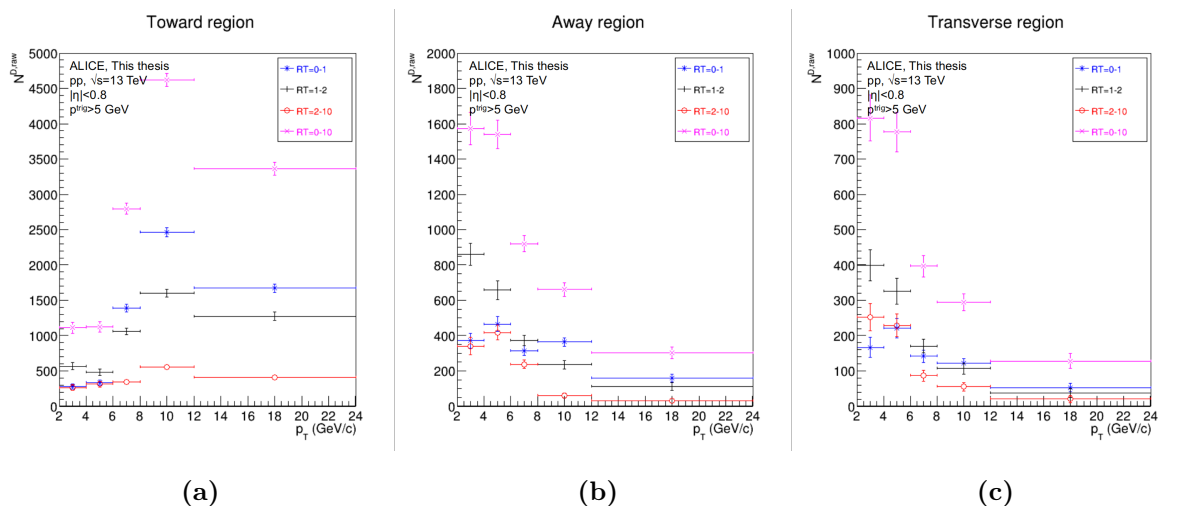

Figure 37: Particle production with the mid-rapidity multiplicity estimator.

To better understand the dependence of D^0 meson production on the underlying event, I combined the three regions and normalized the D^0-meson yields in each R_T range with the R_T-integrated yields. The normalized yields are drawn in function of p_T in Fig. 38. Here one can see, that high-p_T D^0 mesons are mostly created in the events with lower-than-average transverse multiplicity ($R_T < 1$), while the lowest number of yields is observed in events with high transverse activity. Note that these results are not corrected for acceptance, efficiency and feed-down. Because of the normalization, the overall acceptance and efficiency dependence cancels, however, the residual R_T-dependence of these corrections may influence the results. Also, a 15-20% feed-down from B-mesons is contained [41].

Nevertheless, the results allow for a rough comparison of R_T-differential heavy flavor

36
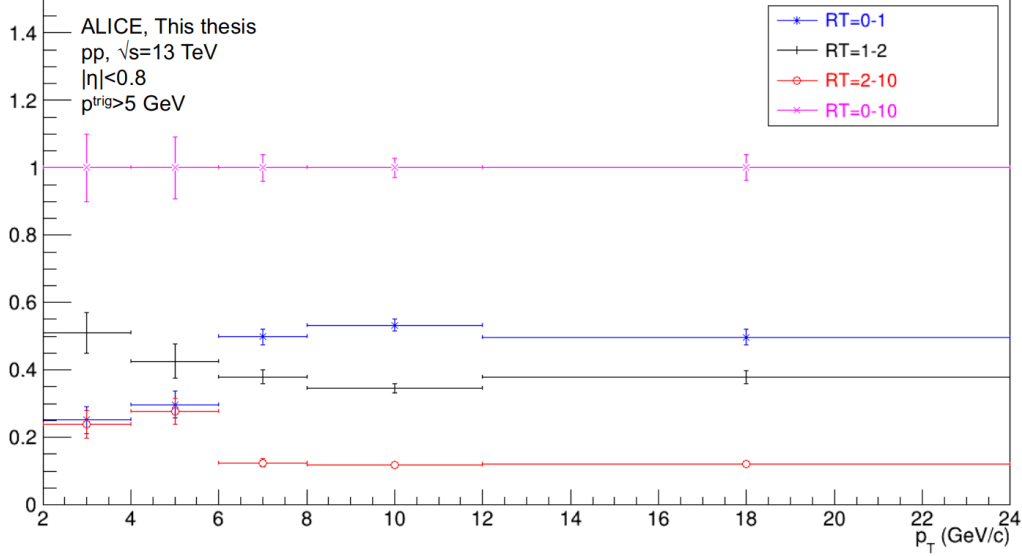
Figure 38: Self-normalized D^0 yields within different R_T intervals.

production to measurements of light flavors performed in ALICE [30] (Fig. 18). As heavy flavor particles are mostly produced in jet regions, the production of heavy particles in the total 4π angle is dominated by the behaviour of light flavor particles in the toward region. This exact behavior is observed in Fig. 38: in events with $R_T<1$ the production ratio of particles increases with their transverse momentum, while in events with high transverse activity ($R_T>2$) the fraction of D^0 yields drops.

In Fig. 39 the self-normalized D^0 yields are shown as function of R_T for the transverse momentum region $2<p_T<8$ GeV/c. An unexpected drop in the toward region, as well as for the $2<R_T<10$ interval can be observed.

The drop in the 2-10 R_T interval is an unexpected result. This can partly be explained by the fact that efficiencies can differ in the jet and the underlying event regions: finding the secondary vertex can be dependent on the multiplicity of its environment. However, the trends can be considered representative and allow me to conclude about the difference in particle production in different regions. As it was discussed in Sec. 2.4, the multiplicity in transverse region should rise steeply because of the autocorrelation events, unlike the charged particle production in the toward region. We see a qualitatively similar behavior from the results in Fig. 39, as the relative number of yields in transverse region becomes bigger than in the toward region with increase in the event activity R_T.
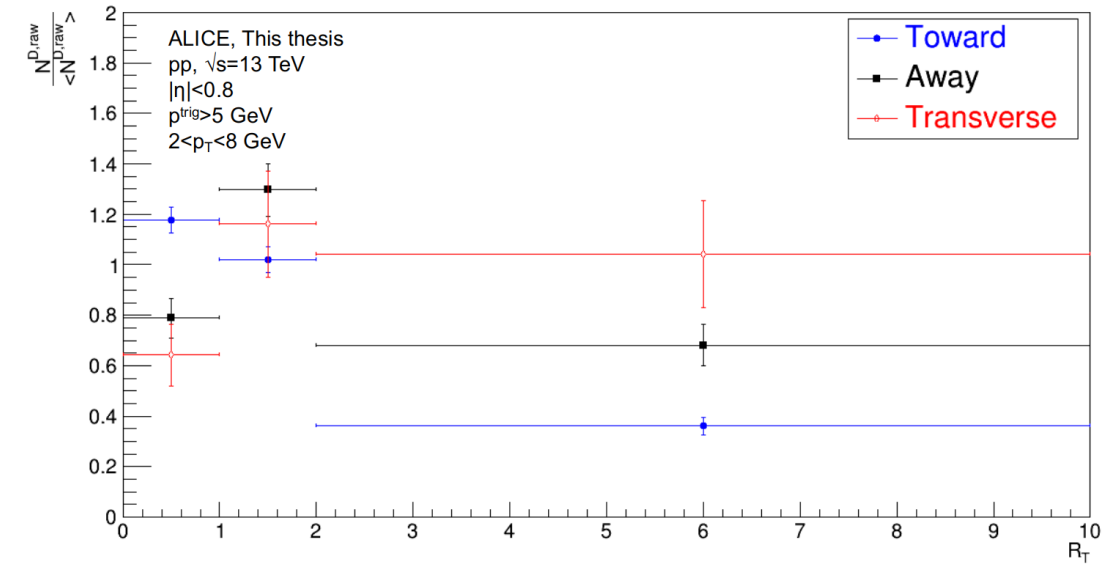
Figure 39: Self-normalized D^0 yields as function of R_T in different azimuthal regions.

6 Summary

This thesis presents a measurement on the transverse event activity dependence of D^0 meson production in proton-proton collisions at $\sqrt{s}$=13 TeV center-of-mass energy that I carried out with the ALICE experiment at the LHC. In collisions of small systems, heavy flavor probes (such as D^0 production) provide a unique opportunity to disentangle different soft and hard Quantum Chromodynamics effects, such as parton production and flavor-dependent fragmentation. Their dependence on the underlying event sheds light on the role of multiparticle interactions and its connection to the structure of the jets, and may reveal the origin of collectivity in high-multiplicity events. In my thesis I describe the ALICE detector systems and I summarize the analysis steps including particle reconstruction and the correction of the raw results, and then I present the the acceptance and efficiency-corrected D^0 meson yields in proton-proton collisions at $\sqrt{s}$=13 TeV in function of the transverse momentum. Although these results are not corrected for feed-down from B mesons, they are consistent with results from previous ALICE measurements. The second part of my analysis concentrates on the classification of reconstructed D^0 mesons by the event activity, using the self-normalized transverse multiplicity R_{T}. The R_{T} dependent efficiency corrections still have to be developed to obtain final results, however, qualitative conclusions can be drawn from the partly corrected results. In correspondence with the results obtained for light charged particles, we see that the R_{T} event classifier can distinguish between the soft and hard events. The final results will allow for a quantitative comparison of the underlying events with light- and heavy-flavor leading partons and their relation to the jet structure. In the future, the R_{T}-dependent analysis could be extended to the B meson production, which may further disentangle mass and flavor-dependent QCD effects.

7   References

[1] Wikipedia, https://en.wikipedia.org/wiki/Standard_Model.

[2] S. Chatrchyan et al., *Observation of a New Boson at a Mass of 125 GeV with the CMS Experiment at the LHC*, Phys. Lett. B **716**, 30-61 (2012).

[3] G. Aad et al. [ATLAS], *Observation of a new particle in the search for the Standard Model Higgs boson with the ATLAS detector at the LHC*, Phys. Lett. B **716**, 1-29 (2012).

[4] M. Breidenbach et al., *Observed Behavior of Highly Inelastic Electron–Proton Scattering*, Phys. Rev. Lett. **23**, 325 (1969)

[5] Craig D. Roberts, *Three Lectures on Hadron Physics*, J. Phys. Conf. Ser. **706**, no.2, 022003 (2016).

[6] E. V. Shuryak, *Quantum Chromodynamics and the Theory of Superdense Matter*, Phys. Rept. **61**, 71-158 (1980).

[7] http://alicematters.web.cern.ch/?q=content/node/1025.

[8] T. Nayak, *Search for the QCD Critical Point at RHIC: First Experience with Au-Au Collisions at 9.2 GeV*, RHIC News, April 8, 2008 edition.

[9] K. Adcox et al. [PHENIX], *Suppression of hadrons with large transverse momentum in central Au+Au collisions at $\sqrt{s_{NN}}$ = 130-GeV*, Phys. Rev. Lett. **88**, 022301 (2002).

[10] P. Jacobs, J. Klay, *Jets and high p_T hadrons in dense matter: recent results from STAR*, AIP Conference Proceedings 698, 667 (2004).

[11] U. A. Wiedemann, *Jet Quenching in Heavy Ion Collisions*, Landolt-Bornstein **23**, 521 (2010).

[12] C. Adler et al., *Disappearance of Back-To-Back High-p_T Hadron Correlations in Central Au+Au Collisions at $\sqrt{s_{NN}}$=200 GeV*, Phys. Rev. Lett. **90**, 082302 (2003).

[13] PHENIX Collaboration, *Enhanced production of direct photons in Au + Au collisions at $\sqrt{s_{NN}}$ =200 GeV and implications for the initial temperature*, Phys. Rev. Lett. **104** (2010).

[14] J. Adam et al. [ALICE], *Direct photon production in Pb-Pb collisions at $\sqrt{s_{NN}}$= 2.76 TeV*, Phys. Lett. B **754**, 235-248 (2016).

[15] S. Voloshin, Y. Zhang, *Flow Study in Relativistic Nuclear Collisions by Fourier Expansion of Azimuthal Particle Distributions*, Z. Phys. C **70** (1996).

[16] K. Ackermann et al. [STAR], *Elliptic flow in Au + Au collisions at (S(NN))**(1/2) = 130 GeV*, Phys. Rev. Lett. **86**, 402-407 (2001).

[17] K. Aamodt et al. [ALICE], *Elliptic flow of charged particles in Pb-Pb collisions at 2.76 TeV*, Phys. Rev. Lett. **105**, 252302 (2010).

[18] A. Adare et al., *Scaling properties of azimuthal anisotropy in Au+Au and Cu+Cu Collisions at $\sqrt{s_{NN}}$=200 GeV*, Phys. Rev. Lett. **98** (2007).

[19] P. Bozek, W. Broniowski, *Correlations from hydrodynamic flow in p-Pb collisions*, Phys. Lett. B **718**, 1557 (2013).

[20] The CMS collaboration, *Evidence for collectivity in pp collisions at the LHC*, Phys. Lett. B **765**, 193 (2017).

[21] The CMS collaboration, *Long-range and short-range dihadron angular correlations in central PbPb collisions at $\sqrt{s_{NN}} = 2.76$ TeV*, JHEP **07**, 076 (2011).

[22] A. Morsch and the ALICE Collaboration, *Multiple Parton Interactions with ALICE: from pp to p-Pb*, Phys.: Conf. Ser. **535**, 012012 (2014).

[23] C. Charlot, *LHC Physics*, SSHEP17, Sarajevo, 2018 (https://indi.to/PF4Gv).

[24] P. Bartalini et al., *Multi-Parton Interactions at the LHC* (2011), https://arxiv.org/pdf/1111.0469.pdf.

[25] K. Aamodt et al. [ALICE], *The ALICE experiment at the CERN LHC*, JINST **3**, S08002 (2008).

[26] ALICE Collaboration, *Charged-particle production as a function of multiplicity and transverse spherocity in pp collisions at $\sqrt{s} = 5.02$ and 13 TeV*, Eur. Phys. J. C **79** 10, 857 (2019).

[27] Martin, T., Skands, P. and Farrington, S., *Probing collective effects in hadronisation with the extremes of the underlying event*, Eur. Phys. J. C **76**, 299 (2016).

[28] O. Vázquez, *Production of (un-)identified light-flavour hadrons as a function of Underlying Event activity in pp collisions with the ALICE detector*, 11th International Workshop on Multiple Partonic Interactions at the LHC, Prague, 2019 (https://indi.to/K94yB).

[29] V. Zaccolo, *Particle production as a function of underlying-event activity measured with ALICE at the LHC* (2019), https://arxiv.org/pdf/1910.04457.pdf.

[30] V. Zaccolo et al. [ALICE], *Transverse momentum spectra of charged particles as a function of Underlying Event activity in pp at 13 TeV*, ALICE internal analysis note **929** (2019).

[31] V. Zaccolo [ALICE], *Particle production as a function of underlying-event activity*

measured with ALICE at the LHC, In the Proceedings of SQM 2019.

[32] A. Misák, *Investigation of the underlying event with heavy quarks*, Zimányi school, Budapest, 2019, (https://indi.to/nSCNc).

[33] A. Misák, *Háttéresemény vizsgálata nehézkvarkokkal az ALICE kísérletben*, BSc thesis, Budapest University of Technology and Economics, 2020 (https://wigner.hu/∼vertesi/publ/19-Misak_BSc_thesis.pdf).

[34] T. Sjostrand, S. Mrenna and P. Z. Skands, *A Brief Introduction to PYTHIA 8.1*, Comput. Phys. Commun. **178**, 852-867 (2008).

[35] R. Brun, R. Hagelberg, M. Hansroul and J. Lassalle, *Geant: Simulation Program for Particle Physics Experiments. User Guide and Reference Manual*, CERN-DD-78-2-REV.

[36] R. Bala et al. [ALICE], *Measurement of charmed mesons and baryons at central rapidity as a function of multiplicity in proton–proton collisions at $\sqrt{s}$ = 13 TeV*, ALICE internal analysis note **993** (2019).

[37] M. Tanabashi et al. [Particle Data Group], *Review of Particle Physics*, Phys. Rev. D **98**, no.3, 030001 (2018).

[38] M. Puccio [ALICE], *Production of (anti-)(hyper-)nuclei production at LHC energies with ALICE*, talk at the 17th International Conference on Strangeness in Quark Matter, Utrecht, the Netherlands (2017), https://indi.to/k9mzc.

[39] J. Wilkinson, *Analysis of D^0 and D^{*+} -meson production in pp and p–Pb collisions with ALICE at the LHC*, PhD thesis, University of Heidelberg (2016).

[40] M. Mazzilli [ALICE], *Non prompt D-meson measurements with ALICE at the LHC*, EPJ Web Conf. **129**, 00033 (2016).

A Invariant mass distributions of D^0 mesons in different R_T intervals
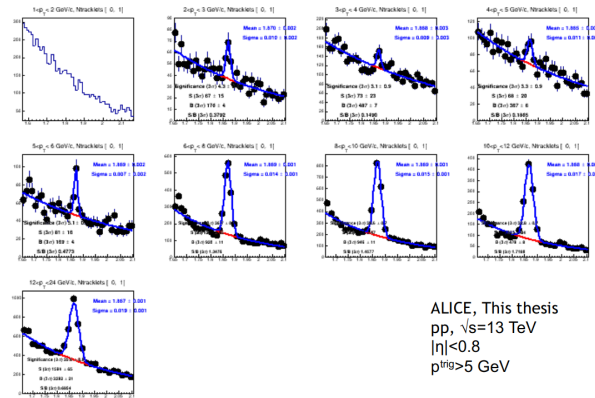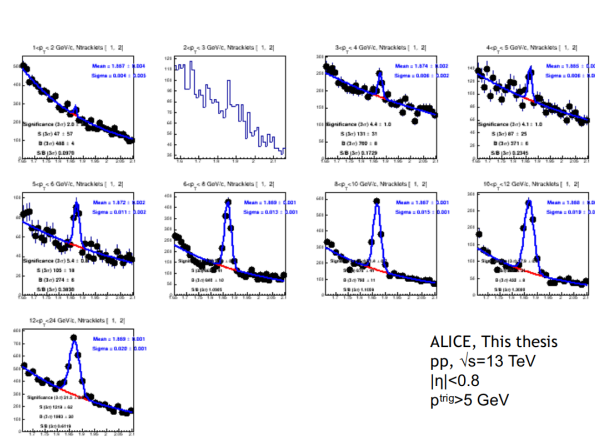

Figure 40: Toward region, R_T=0-1.
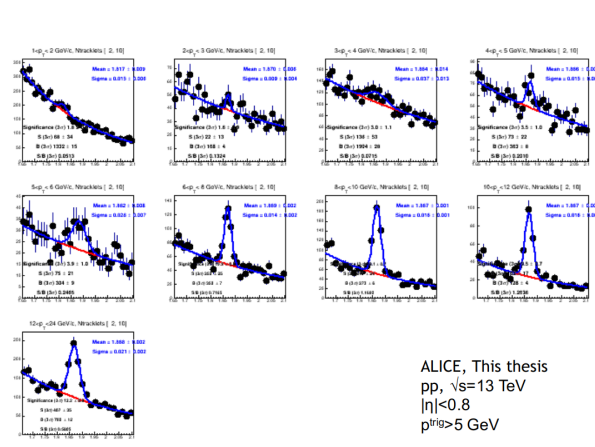

Figure 41: Toward region, R_T=1-2.
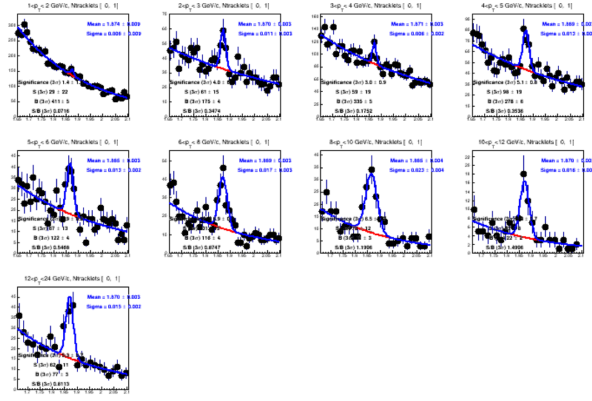

Figure 42: Toward region, R_T=2-10.
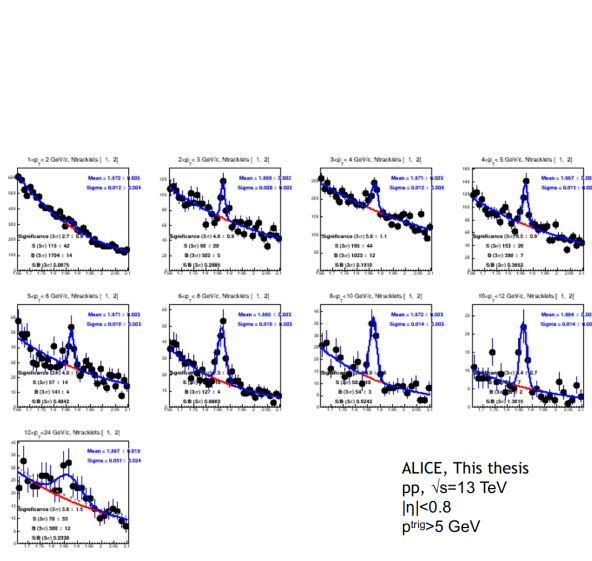
Figure 43: Away region, R_T=0-1.

Figure 44: Away region, R_T=1-2.
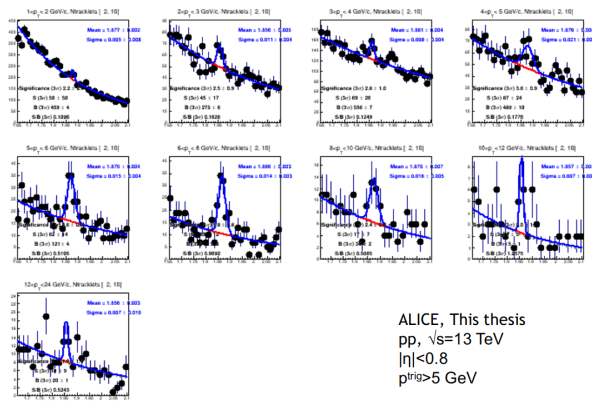
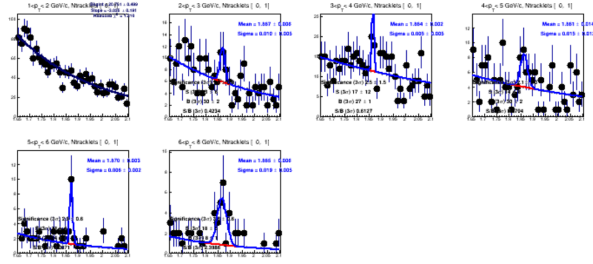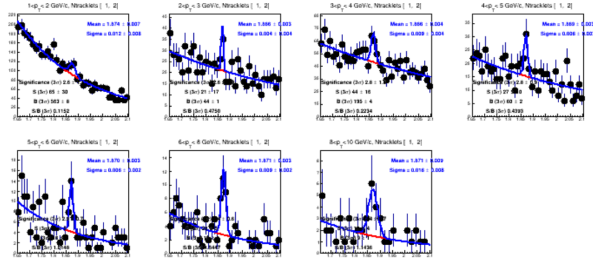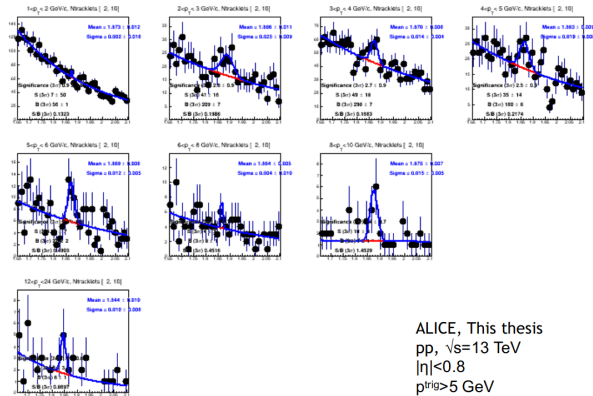**Figure 45:** Away region, R_T=2-10.

45

Figure 46: Transverse region, R_{T}=0-1.

Figure 47: Transverse region, R_{T}=1-2.

Figure 48: Transverse region, R_{T}=2-10.